Wind Profiling Portable Radar (WiPPR)

Marshall Bradley, Mark Henderson and Michael Vollmuth
LogLinear Group

Quinn Smith
QinetiQ Inc.

Introduction

The LogLinear Group and Qinetiq have developed a new type of low noise, wide band, frequency modulated continuous wave (FMCW) radar capable of detecting clear air scatter in the convective boundary layer. We refer to this technology as the Wind Profiling Portable Radar (WiPPR). Development of the system began in 2010 and continued until 2016 when the focus of our efforts shifted from ground-based to airborne radar operations. This latter effort led to the development of the AWiPPR system. As of 2021 the radar hardware improvements developed for AWiPPR have been incorporated into WiPPR. This document does not address AWiPPR directly.

The radar operates at a carrier frequency of f_c = 33.4 GHz in the Ka band. Originally selectable linear sweep widths of 6, 12, 24, 36 and 48 MHz were employed. As of 2021 the radar uses a fixed 48 MHz sweep width. The size of the sweep width controls the range resolution of the radar and it was thought that advantages could be obtained by matching the sweep width the radar to scattering characteristics of the target. This is the case for volumetric targets like hydrometers but not for point targets. After an extensive field testing program it was determined that the 48 MHz sweep width provided good performance against all target types.

The radar can detect clear air scatter targets at altitudes up to 1500-2000 m. This altitude range represents the upper limits of the convective boundary layer (also called atmospheric boundary layer). These clear air scatterers are turbulent motions of the air associated with ever-present hydrodynamic- thermodynamic instabilities in the atmosphere. We have observed these phenomena all over the continental US. Their prevalence is most pronounced during time periods when solar illumination is high and the atmosphere is unstable. This turbulence is also present during stable atmospheric conditions but usually at lower altitudes. The radar can also detect trace precipitation, rainfall, and certain types of clouds. WiPPR radar data can also be processed to produced turbulent intensity as a function of altitude. This quantity is important in wind pressure loading problems.

This document provides a detailed description of the physics supporting the WiPPR system and contains many examples of WiPPR performance.

Theoretical Considerations

At the beginning of the WiPPR program our design goal was to detect a clear air target with a -30 dBZ reflectivity up to the top of the convective boundary layer (1500m). This section presents several theoretical discussions related to building a radar with this capability.

The figure to the right shows the performance of a radar with characteristics similar to those of the WiPPR system against clear air (-30 dBZ), heavy stratus clouds (-12 dBZ) and drizzle (14 dBZ) targets. Specific values used in the computations are 3 W transmit power, 37 dB gain antennas' stack size of 256, 190 micro-sec pulse, 48 MHz sweep, and a system noise temperature of 130 degK

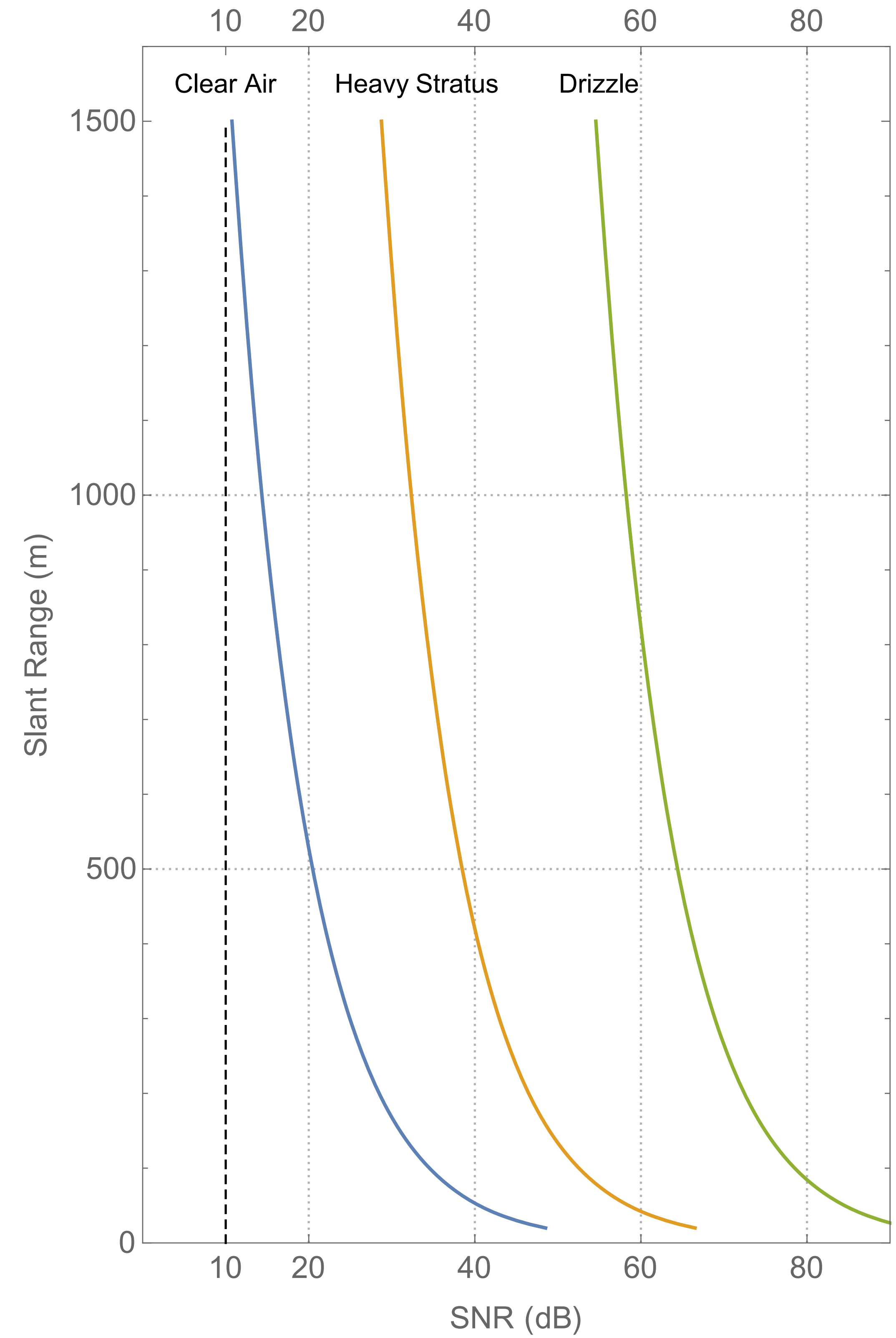

Selection of Carrier Frequency

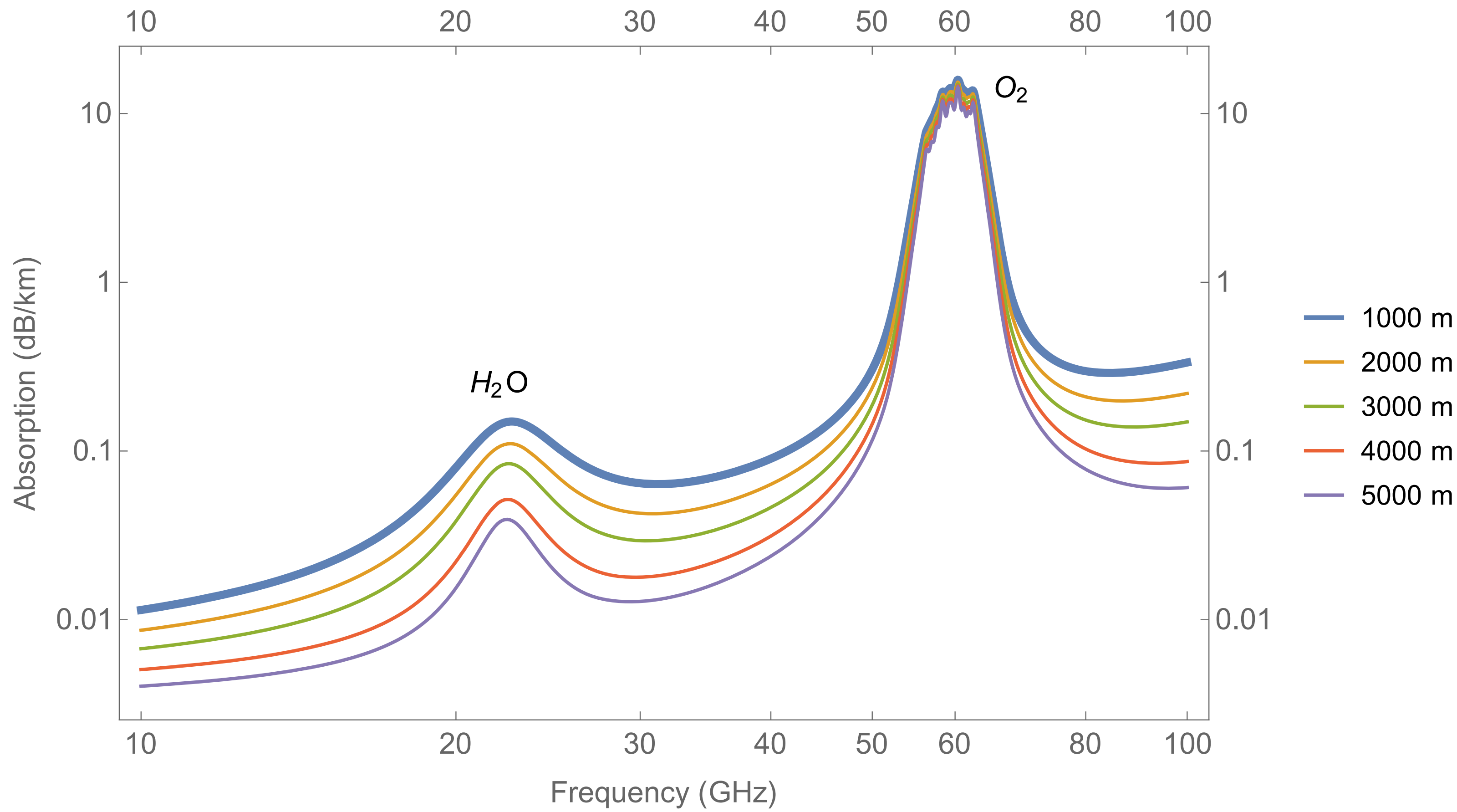

Atmospheric radar wave absorption over the altitude range 1000-5000 m.

A fundamental design consideration for a radar is the choice of carrier frequency. The WiPPR signal needs to propagate up to the top of the convective boundary layer (CBL) and back without suffering large absorption losses. This is nominally a round trip distance of 3 km. Absorption of propagating radar waves in the atmosphere in the range 10-100 GHz is greatest at 22 GHz and 60 GHz due to absorption by water vapor molecules (22 GHz) and by oxygen molecules (60 GHz). For a fixed frequency, absorption is less at higher elevations than at lower elevations. Two-way absorption losses to the top of the CBL and back at 33.4 GHz, 60 GHz and 80 GHz are respectively 0.21 dB/km, 44 dB/km and 0.97 dB/km. It is obviously vital to avoid the oxygen absorption at 60 GHz. A carrier frequency of 33.4 GHz was chosen for WiPPR because of its low absorption and the slight advantage it presented over frequencies in the 80-100 GHz range during periods of rainfall. Falling hydrometers introduce additional absorption which is lower at 33.4 GHz that at frequencies in the 80-100 GHz band.

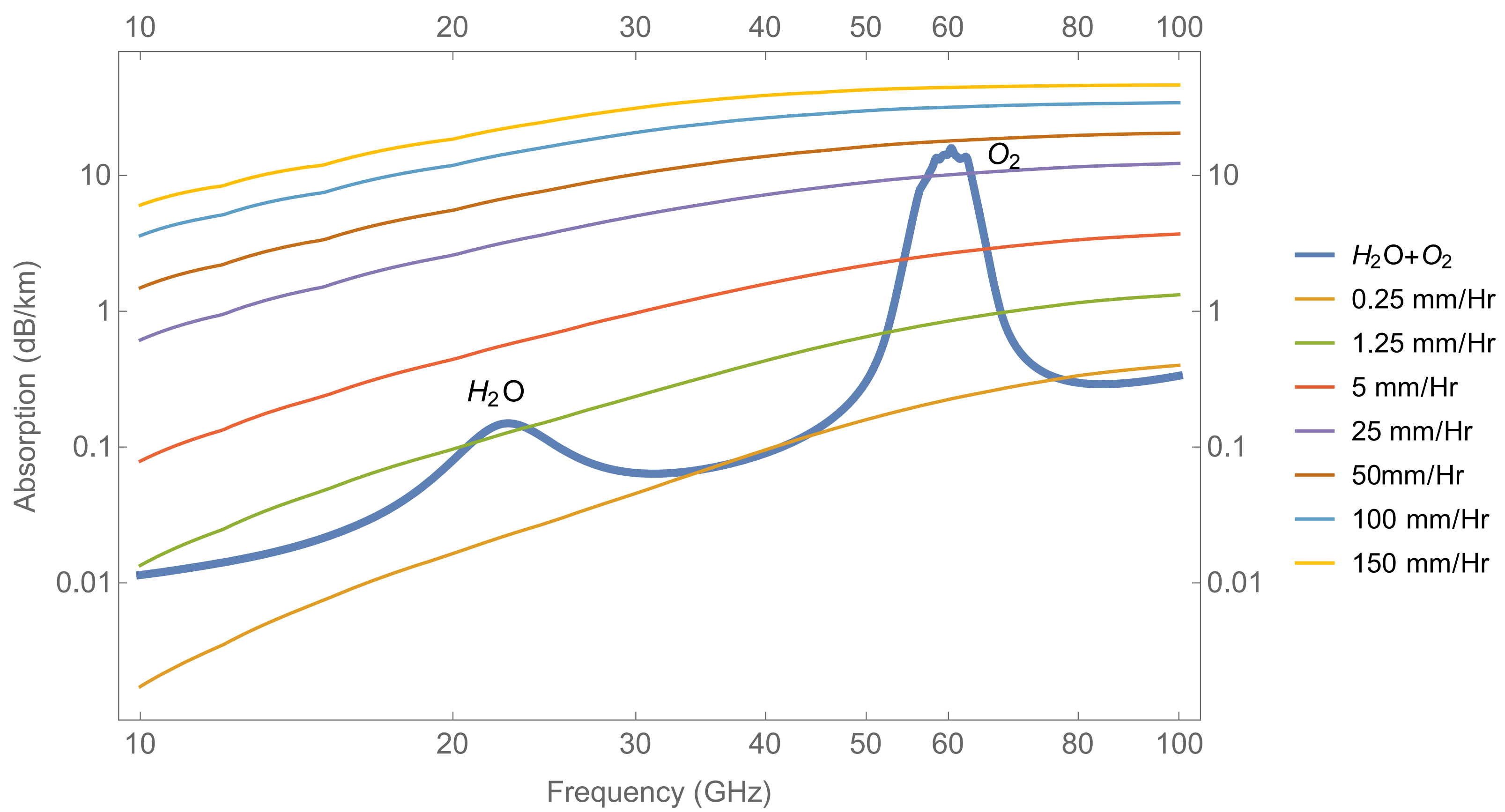

Atmospheric absorption due to water vapor and oxygen compared to absorption from rainfall.

The thick blue line is atmospheric absorption from water vapor and oxygen. The black lines show additional absorption from rainfall at various rainfall rates. A radar operating near 33 GHz clearly has an advantage over an 80-100 GHz radar in terms of the additional absorption from rainfall at the higher frequencies.

Radar Equation

We consider radar with transmit power P_t employing a pair of identical, nearly colocated transmit and receive antennas each with gain G measured on a power scale. The solid angle illuminated by the antennas is $\Omega = 4\pi/G$. A target is located at a distance r from the antennas in the direction of peak radar response. The radar cross-section of the target is denoted by σ_{RCS}. The power flux density in the direction of the radar's main beam axis at the target location is

$$F_{tgt} = \frac{GP_t}{4\pi r^2}$$

The power received by targets is $F_{tgt}\sigma_{RCS}$. This energy radiates back to the receiver where the flux density is

$$F_r = \frac{GP_t\sigma_{RCS}}{(4\pi)^2 r^4}$$

The power received by the reciter antenna is

$$P_r = \frac{GP_t\sigma_{RCS}A_e}{(4\pi)^2 r^4}$$

where A_e is the effective area of the receiver antenna. This equation can be further simplified by noting the relationship between the gain G of the receiver antenna and its effective area A_e

$$A_e = \frac{G\lambda^2}{4\pi}$$

where λ is the wavelength of the carrier frequency of the radar. The received power from the target echo can now be written in the form

$$P_r = P_t\frac{G^2\lambda^2\sigma_{RCS}}{(4\pi)^3 r^4}$$

This equation is usually referred to as the radar equation. It is nothing more than conservation of energy. If we include the effects of atmospheric absorption then the radar equation becomes

$$P_r = P_t\frac{G^2\lambda^2\sigma_{RCS}}{(4\pi)^3 r^4}10^{-2\alpha r/10}$$

where α is absorption loss measured in units of dB per unit distance. If the radar receiver employ a matched filter then the signal to noise ratio of the echo is $SNR = T_m P_r/N_0$ where T_m is the radar pule length and N_0 is the noise power spectra density (power/Hz) in the detector band.

If the target is a distribution of falling hydrometers then the radar equation must be modified. If B denotes the bandwidth of the FM sweep used by the radar and c is the speed light, then the volume illuminated by the radar pulse is

$$V = \Omega r^2 (c/2B)$$

where $\Omega = 4\pi/G$ is the solid angle illuminated by the radar. The quantity $c/(2B)$ is the extension of the radar pulse in range. The target radar radar cross section is

$$\sigma_{RCS} = \Omega r^2 (c/2B)\eta$$

where η is a backscatter coefficient measured is units of inverse length. With these definitions the radar equation becomes

$$P_r = P_t \frac{G^2 \lambda^2}{(4\pi)^3 r^2} \Omega (c/2B) \eta 10^{-2\alpha r/10}$$

An important point here is that for a volumetric target spending loss in the radar equations varies like r^{-2} and not r^{-4}. Additionally target radar cross section should increase if the transmit pulse bandwidth decreases.

In terms of the dBZ backscatter scale used in the meteorology community

$$\eta = \frac{10^{-18} K^2 \pi^5 10^{dBZ/10}}{\lambda^4}$$

where $K = (0.93)^{1/2}$ is a dimensional constant and distances must be measured in meters.

Ultimately radar performance is limited by thermal noise. The thermal noise spectral density N_0 (W/Hz) of an idealized radar with electronics at temperature T_{elec} is $N_0 = k_B T_{elec}$ where k_B is the Boltzmann constant $1.38\ 10^{-23}$ J/K. Practical electronic circuits are not able to achieve the thermal noise limit. A better representation of the noise spectral density that sets the upper limit on radar performance is

$$N_0 = k_B T_{elec} 10^{\text{NoiseGain}/10}$$

where NoiseGain is the noise gain of the radar electronic measure in dB re the thermal noise limit. Nominal values for NoiseGain are in the 6 to 9 dB range.

FMCW Radar Data Processing

The following discussion presents a brief, high-level overview of the signal processing used by frequency modulated continuous wave (FMCW) radar to resolve a targets range and velocity. The sweep width and pulse length of the radar are respectively denoted by B and T_m. A target is located at a distance r_0 from the radar and is moving with a radial velocity v_0 towards the radar . The echo time delay of the target is

$$\tau = 2r_0/c$$

where c is the speed of light . The target beat frequency of the radar is

$$f_{beat} = \frac{\tau}{T_m}B = \frac{2r_0}{cT_m}B$$

Physically the beat frequency signal is produced by mixing the transmit signal with the received signal and low-pass filtering to keep only the down mix. Targets at greater ranges produce higher beat frequencies. The analytic form of the echo from the target is proportional to

$$s(t) = \exp(-j2\pi f_{beat}t)$$

The radar detects the range to the target via Fourier analysis of the echo signal. This results in the echo range representation

$$S_{range}(f) = \int_0^{T_m} \exp(-j2\pi f_{beat}t)\exp(j2\pi ft)dt$$

The integral can be evaluated in closed form to yield

$$S_{range}(f) = C_0\text{sinc}[\pi(f - f_{beat})T_m]$$

where C_0 is a constant that does not depend on the frequency f. If we make the substitution $f = (2r/cT_m)B$ then we obtain

$$S_{range}(r) = C_0\text{sinc}[\pi(r - r_0)B]$$

and we see that the sweep width B controls the sharpness of the spectral peak. If we take the time to evaluate the constant C_0 we obtain

$$S_{range}(r) = \exp[j\pi\frac{2}{c}(r - r_0)]\text{sinc}[\pi(r - r_0)B]$$

The Doppler shift of the target is $f_d = 2v_0/\lambda$ where λ is the radar carrier frequency wavelength.

Slow time radar data obtained from Q pulses each of length T_m behaves in phase like

$$s_q = \exp(-j2\pi f_d T_m q)$$

where $q = 0,1,2,...Q-1$. The Doppler phase shift of the target relative to the radar can be found by employing a Fast Fourier Transform (FFT). This leads to

$$S_{velocity}(f) = Q^{-1/2}\sum_{q=0}^{Q-1}\exp[j2\pi(f-f_d)T_m q]$$

If we define the phase shift α to be $\alpha = 2\pi(f-f_d)T_m$ then the FFT can be summed in closed form to produce

$$S_{velocity}(v) = C_1\frac{\sin(Q\pi\alpha/2)}{\sin(\pi\alpha/2)} = C_1\frac{\sin[Q\pi(v-v_d)/v_{max}]}{\sin[\pi(v-v_d)/v_{max}]}$$

where C_1 is a constant that does not depend on frequency and $v_{max} = \lambda F_m/2$, $F_m = 1/T_m$. A combined target range-Doppler velocity response of the radar signal processing or more precisely the ambiguity function of the radar is

$$S_{radar}(r, v\,|\,r_0, v_0, B, Q) = S_{range}(r)S_{velcoty}(v)$$

where r is the radar signal processor search range, v is the search velocity, r_0 is the target range and, v_0 is the target radial velocity, B is the radar FM sweep width and Q is the number of pulses used by the radar. In deriving the range response of the radar we considered time t to be a continuous variable. If the radar samples the output of the mixer at discreet times t_j defined by

$$t_j = j\frac{T_m}{M},\ j = 0,1,2,...M-1$$

where T_m is the radar pulse length and M is the number of times an individual pulse is sampled, then the discrete sampling approach for the range response the radar range-velocity ambiguity function becomes

$$\frac{\sin[M\pi(r-r_0)/2r_{max}]}{\sin[\pi(r-r_0)/2r_{max}]}\frac{\sin[Q\pi(v-v_d)/v_{max}]}{\sin[\pi(v-v_d)/v_{max}]}$$

where the maximum unambiguous range of the radar is

$$r_{max} = \frac{c}{2B}\frac{M}{2}$$

As (r, v) tends to (r_0, v_d) the ambiguity function produces a peak response of MQ, which is the processing gain relative to an input signal with unit amplitude.

WiPPR Signal to Noise Ratio

For an FMCW radar with pulse length T_m and sweep width B, a target located at the range $r_m = m_r(c/2B)$ will produce an echo of the form

$$s(t) = a\,\exp(-j2\pi m_r F_m t)$$

where m_r is the range index of the target, $F_m = 1/T_m$ is the radar pulse frequency and a is the echo amplitude. In terms of the radar equation relating radar transit power P_{tx} to received power P_{rx}, the echo amplitude a is effectively defined by

$$a^2 = P_{rx} = \frac{P_{tx} G^2 \lambda^2 \sigma_{RCS}}{(4\pi)^3 r^4}$$

where G is the radar antenna gain, λ is the carrier frequency wavelength and σ_{RCS} is the target radar cross section. If we adopt the Fast Fourier Transform normalizing convention shown in the following equation:

$$B_n = M^{-1/2} \sum_{m=0}^{M-1} A_m \exp(j2\pi mn/M)$$

then the target echo out of the range FFT will have amplitude $aM^{1/2}$. If target velocity determination is accomplished with an FFT of length Q using a similar normalization, then the amplitude of the target echo increases to $aM^{1/2}Q^{1/2}$ with corresponding power a^2MQ.

The final step in the WiPPR range velocity matrix formation process is to power average multiple range velocity matrices in order to reduce the variance of the background noise level in each individual range-Doppler velocity cell. If N range velocity matrices (measured on a power scale) are averaged together, then the target echo remains unchanged so that the received echo power including processing gain is

$$P_{rx} = MQ\frac{P_{tx} G^2 \lambda^2 \sigma}{(4\pi)^3 r^4}$$

The foregoing assumes the target echo remains constant during the time interval NT_mQ. The system bandwidth required to support target detection out to the maximum range $r_{max} = (M/2)(c/2B)$ is $B_{system} = MF_m$. The total noise power in this band is

$$\sigma^2 = k_B T_{system} B_{system}$$

where k_B is the Boltzmann constant $1.38\ 10^{-23}$ J/K and T_{system} is the system noise temperature.

The range FFT produces noise with noise power in each range FFT cell given by

$$\sigma_r^2 = \frac{1}{M}(\sigma^2 + \sigma^2 \ldots + \sigma^2) = \sigma^2$$

where the above sum has M terms. A similar result holds for the Doppler velocity FFT. Thus the noise power in a single range-Doppler velocity pixel of an individual WiPPR range velocity matrix is $\sigma^2 = k_B T_{system} B_{system}$. Increasing the FFT sizes M or Q does nothing to increase signal to noise ratio.

The exact statistical distribution of the noise in a range-Doppler velocity bin is exponential. This probability density distribution of this function is

$$p(x\,|\,\sigma^2) = \sigma^{-2} \exp(-x/\sigma^2),\ x > 0$$

where x denotes the noise power in a cell. Averaging N independent exponential random variables produces a gamma distributed random variable with mean σ^2 and standard deviation $\sigma^2/N^{1/2}$. For large N the gamma distribution is approximately normally distributed.

Thus for large N the noise distribution in a range-Doppler cell is effectively normally distributed with mean σ^2 and standard deviation $\sigma^2/N^{1/2}$. Increasing the size of N reduces the fluctuations in the background noise in the cell and facilitates the detection of weak echos. An approximate model for the detection process is that the signal echo power must me greater than the noise mean plus two standard deviations of noise. This leads to the following form of the radar equation for WiPPR

$$SNR = \frac{MQa^2}{\sigma^2 + 2\sigma^2/N^{1/2}} = \frac{QT_m a^2}{(1 + 2/N^{1/2})k_B T_{system}}$$

This equation implies that SNR is enhanced by using a larger pulse length T_m., using a larger stack size Q, reducing system noise temperature T_{system} or performing more averaging (larger N). The effects of larger averaging rapidly saturate. Increasing the pulse length T_m reduces the range of doppler velocities that the system can unambiguously recognize.

Universal Probability Density Function of Detected SNR

In the following discussion we derive the universal probability density function for the distribution of detected SNR values and show how this probability density function (PDF) can be used to estimate the slant range decay rate of radar echoes due to reflection from clear air scatter. By decay rate we mean the way in which radar echoes diminish in power as a function of slant range r. Specifically we consider the case in which the decay as a function of slant range is given by r^{-a} where a is a constant. The approach that we take here is adapted from Schutz (2011) who was concerned with the passive detection of gravitational waves. From the stand point of signal processing, there are strong similarities between the passive detection of gravitational waves and the active detection of radar echoes. By detected signal to noise ratio (SNR) we refer to radar echoes that are above a threshold that is large enough to insure that the echo is produced by reflection from a target and is not just a spike in the background noise level.

The SNR of a radar echo can be written in the simplified form

$$y = F/r^a$$

where the symbol y denotes the SNR of the echo measured on a power scale, F is the figure of merit of the radar, r is the radial distance (or slant range) to the target and a is the decay rate constant. The cases a=1,2 and 4 respectively refer to the passive detection of an advancing cylindrical wave, the weather radar equation and the ordinary radar equation. For this last case

$$F = T_m \frac{P_t G^2 \sigma_{RCS} \lambda^2}{(4\pi)^3 T_{system} k_B}$$

where T_m is the radar pulse length, P_t is transmit power, G is the antenna gain, λ is carrier frequency wavelength, T_{system} is the effective radar system noise temperature and k_B is the Boltzmann constant. If y_T denotes the threshold SNR for the radar, then the maximum range at which the radar can make a detection is $r_{max} = (F/y_T)^{1/a}$.

If β denotes the constant density per unit volume of targets, then the number of detections produced by the radar at the two SNR thresholds y_T and $y > y_T$ is

$$N_D(y_T) = \beta\Omega(F/y_T)^{3/a}, \; N_D(y) = \beta\Omega(F/y)^{3/a}$$

where Ω is the solid angle subtended by the radar beam. If the radar is omnidirectional and the entire hemisphere is illuminated then $\Omega = 2\pi$. In general $\Omega = 4\pi/G$.

The fraction of targets that are detected at SNR values $y > y_T$ is the ratio of these two quantities, i.e

fraction detected $= (y_T/y)^{3/a}$

If $y = y_T$ the fraction of targets detected is unity. The cumulative fraction of targets detected as a function of the SNR value y is

$$G(y) = 1 - (y_T/y)^{3/a},\ y > y_T$$

At this point it is convenient to make a change in notation that simplifies the analysis that follows. The change that we make is to define $\alpha = 3/a$. As the parameter a assumes the values 1,2 and 4 then α becomes 3, 3/2 and 3/4. With this change in notation, the cumulative fraction of targets detected as a function of the SNR value y is

$$G(y) = 1 - (y_T/y)^{\alpha},\ y > y_T$$

and zero otherwise. The function $G(y)$ is the cumulative probability density function of a Pareto random variable with probability density function $g(y)$ defined by

$$g(y) = \frac{d}{dy}G(y) = \alpha y_T^{\alpha} y^{-\alpha-1},\ y > y_T$$

and zero otherwise. When $\alpha = 3$ corresponding to the scalar (not power) passive detection of an advancing gravity wave or the passive power detection of a cylindrically spreading acoustic wave, then $g(y) = 3y_T^3 y^{-4}$ for $y > y_T$ and zero otherwise. This is precisely the form obtained by obtained by Schutz (2011). They refer to $g(y)$ as the universal probability density function for the distribution of detected SNR values. The probability density function $g(y)$ does not depend upon the figure of merit F of the radar. The range dependence in the underlying radar equation that governs the propagation physics is encoded in the parameter $\alpha = 3/a$.

The median value of a Pareto distribution with threshold y_T and decay constant α is $2^{1/\alpha}y_T$. This implies that 1/2 of all detections will occur in the SNR range $y_T < y < 2^{1/\alpha}y_T$. For the case $\alpha = 3/2$ (weather radar equation with $a = 2$), 1/2 of detections occur within $10\log_{10} 2^{2/3} = 2$ dB of the threshold y_T. For the ordinary radar equation ($a = 4$), 1/2 of the detections occur within 4 dB of the threshold y_T. Small losses in SNR can have profound effects on the number and rate at which detections occur.

Reference: Schutz, Bernard (2011), "Networks of gravitational wave detectors and three figures of merit ", Classic and Quantum Gravity, Vol. 28, No. 12.

Range Velocity Matrix Formation

The Fundamental Building Block

The fundamental data building block produced by WiPPR is the range velocity matrix. This data structure localizes echo producing objects in slant range-Doppler velocity space and enables the computation of wind velocity profiles. In the range velocity matrix shown to the right the radar has detected echos form clear air scatter (convective turbulence in this case) and falling hydrometers. The hydrometers produce higher Doppler velocity (larger index) because they are moving almost directly towards the near-vertical radar beam. Figure produced using data recorded on 25 February 2014.

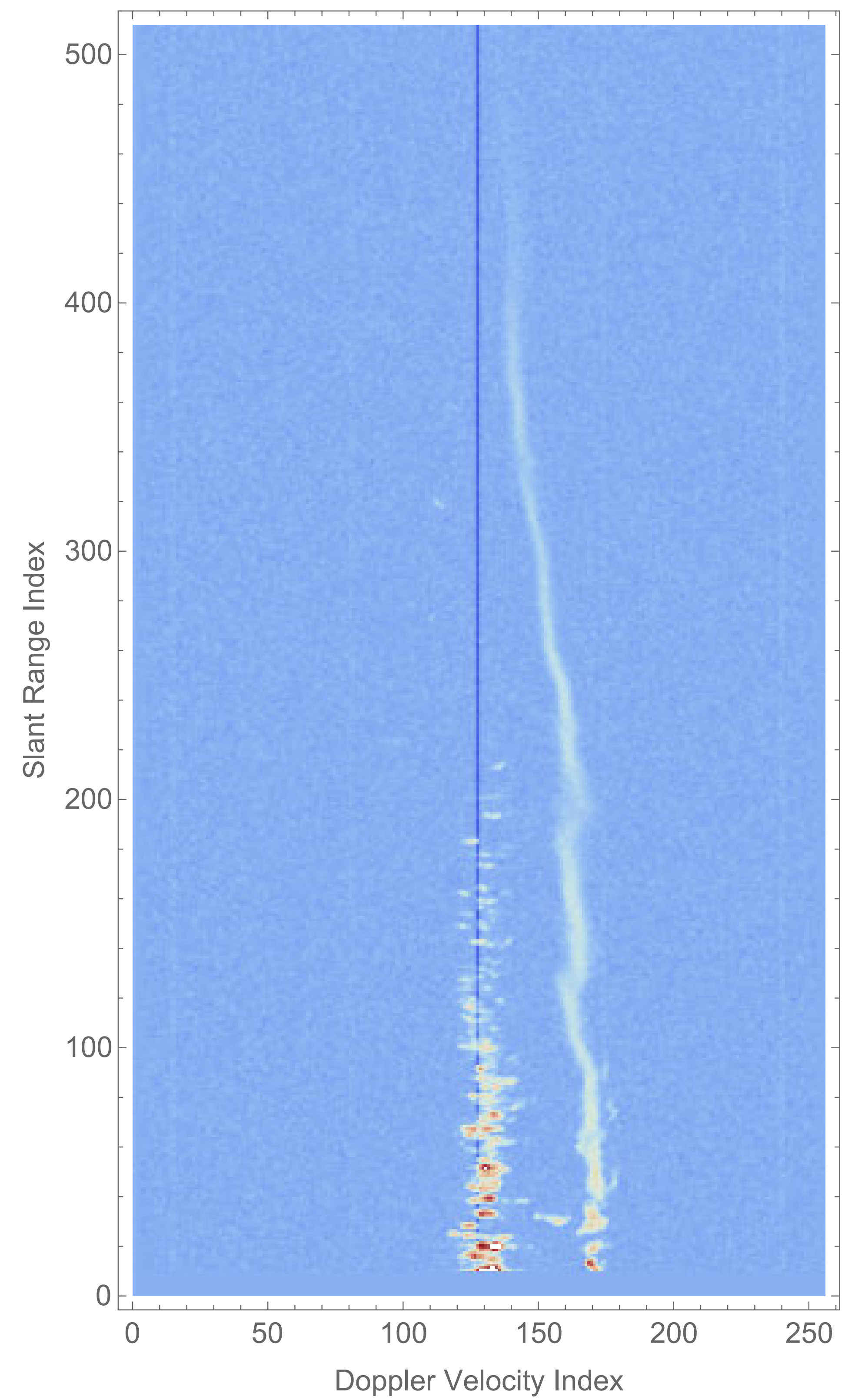

Fast-Time Slow-Time Processing

The WiPPR radar estimates the range and Doppler velocity of a target echo by using a form of fast-time/slow-time processing that produces a range-velocity matrix (or gram). The formation of range-velocity matrices is depicted in figures that follow.

Step a) Raw radar echo data is placed into a data stack (also referred to as a matrix). The individual pulses were each originally $M = 256$ samples long and are located in the vertical columns of the stack. They are now $M = 4096$ samples in length. This is repeated to form the entire data stack. The stack size is $Q = 256$. The vertical axis in the matrix is known as fast time and the horizontal axis is slow time. The time sampling interval in fast time is $\Delta t_{fast} = T_m/M$ where T_m is the radar pulse length. Sampling in slow time is at steps of $\Delta t_{slow} = T_m$. An entire data stack spans the time interval $t_{coherent} = QT_m$. This time interval represents the time over which coherent data processing is performed.

Step b) A Fast Fourier Transform (FFT) is applied to the vertical columns of the stack in order to resolve targets in range. This step resolves the beat frequencies in the down-mixed radar echoes that arise from their round- trip time delay from the radar to the scattering objects and back. In the example shown in the following figure, there is a strong band of echoes near altitude (or range) index 25 with amplitudes that fluctuate in slow time.

Step c) To resolve targets in velocity, FFTs are performed horizontally for each row in the data-matrix shown in step b). The relative power processing gain in moving from step a to step c is MQ.

The data-matrix produced by carrying out steps a-c is referred to as the range-velocity matrix (RVM). The dimensions of the useful information in the RVM are $(M/2 + 1)$ by Q. Hamming windows are applied in both stages of FFTs in order to reduce spectral leakage. If A, B and C denote the images shown in the following figure then

$$B_{rn} = M^{-1/2} \sum_{m=0}^{M-1} w_m A_{mn} e^{j2\pi mn/M},\ r = 0,1,2,\ldots,M-1$$

$$C_{rq} = Q^{-1/2} \sum_{n=0}^{Q-1} w_n B_{rn} e^{j2\pi rn/Q},\ q = 0,1,2,\ldots,Q-1$$

The observed slant range R_r and Doppler velocity V_q corresponding to the location (r, q) in the range velocity matrix C_{rq} are defined via

$$R_r = r\frac{c}{2B},\ r = 0,1,2,\ldots,M/2+1$$

where c is the speed of light and B is the sweep width of the radar. The Doppler velocity at index q is

$$V_q = V_{min} + q\frac{1}{Q-1}\frac{\lambda}{2T_m},\ q = 0,1,2,\ldots,Q-1$$

where λ is the wavelength of the carrier frequency of the radar.

Since both positive and negative Doppler velocities are possible, the actual range of Doppler velocities resolved by fast-time slow-time processing is

$$-\frac{\lambda}{4T_m} < V < \frac{\lambda}{4T_m}$$

and the range-velocity matrix C_{rq} must be rotated with respect to the q index by $Q/2$ to the right. If radar beams are elevated by an angle θ from the horizontal then this range in Doppler corresponds to an unambiguous wind velocity range for horizontally moving winds of

$$(-\frac{\lambda}{4T_m\cos(\theta)}, \frac{\lambda}{4T_m\cos(\theta)}) = (-68.1, 68.1) \text{ m/s}$$

for a pulse length of $T_m = 190$ μsec and a carrier frequency of 33.4 GHz.

Echoes from strong reflectors are easily detectable in the range-velocity matrix C_{rq} but the weak reflections from clear air scatterers and weather events require more processing gain in order to be reliably detectable. This is achieved by spectral averaging as previously discussed. The power averaged range-velocity matrix is specifically calculated via

$$P_{rq} = N^{-1}\sum_{k=1}^{N} |C_{rq}(k)|^2$$

where k corresponds to a time step of length QT_m equal to the time duration of a data stack. The averaging used to form the power averaged range velocity matrix P_{rq} is performed without overlap in time order to maintain statistical independence.

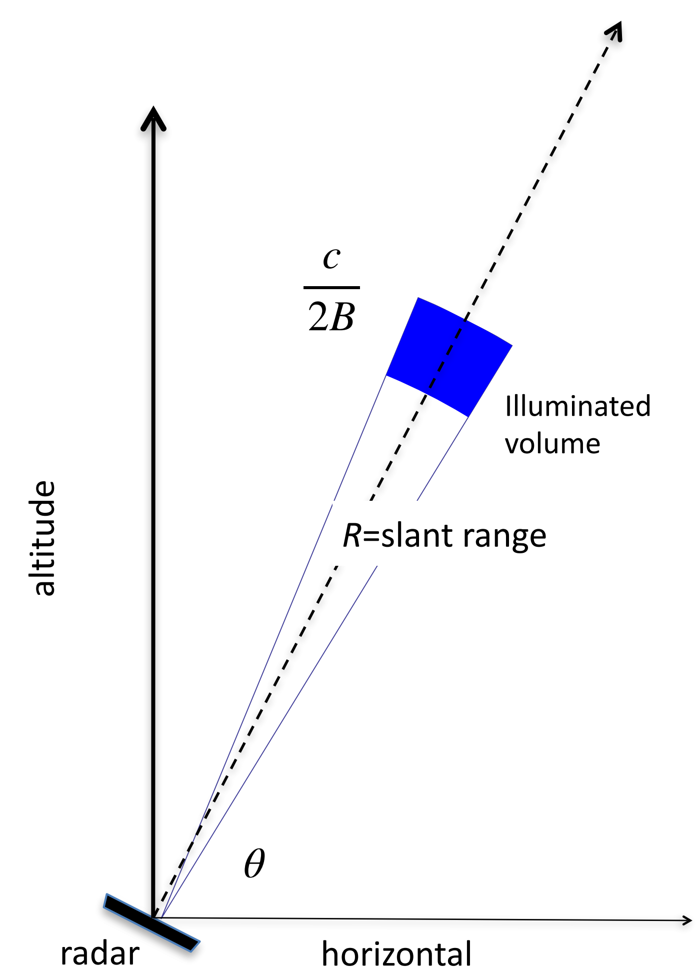

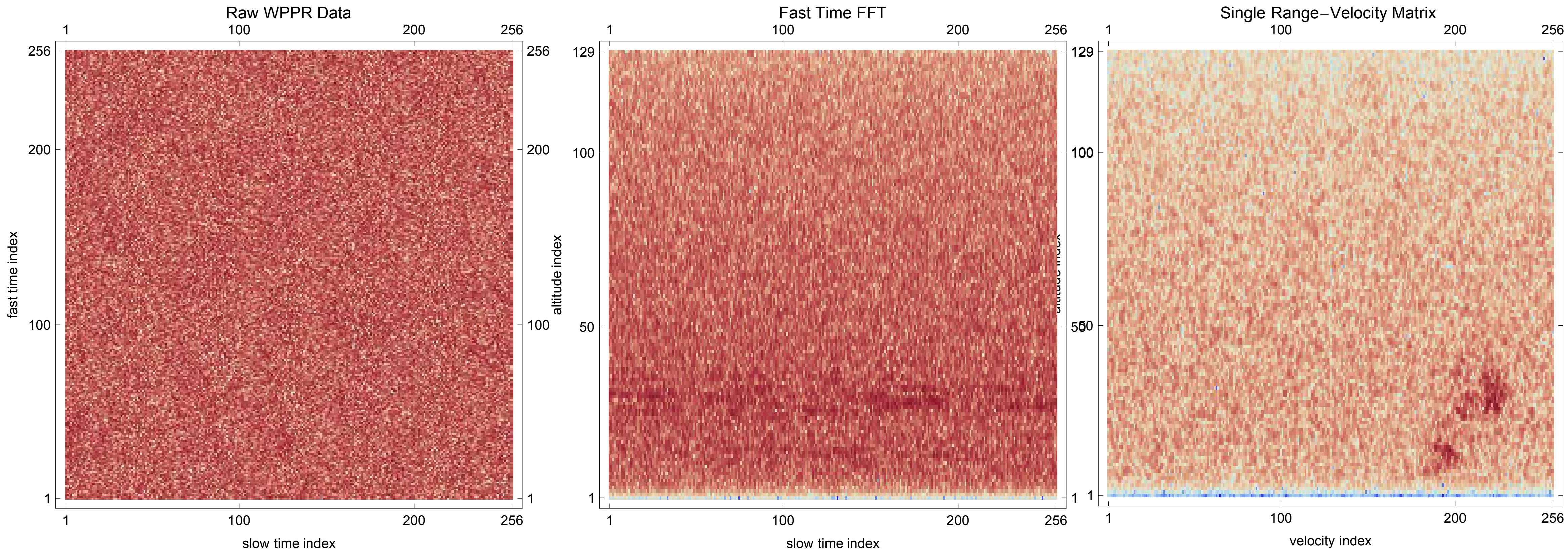

Formation of the range-velocity matrix image using data from the late 2010-early 2011 time period.

Range-velocity matrices are the fundamental building block of WiPPR data processing. Their formation is illustrated here using early WiPPR data when the range FFT size was 256.

Left) Raw WiPPR echo data is placed into a data stack. The individual pulses are each M=256 samples long and are located in the vertical columns. This is repeated to form the data stack. In this case the stack size is also Q=256. The vertical axis in the matrix is known as fast time and the horizontal axis is slow time. The time sampling interval in fast time is T_m/M where T_m is the radar pulse length. Sampling in slow time is at steps of T_m. The stack size Q was originally selectable but Q=256 was fixed early in the project development.

Center) An FFT is applied to the vertical columns of a) in order to resolve targets in range. This step resolves the beat frequencies in the down-mixed radar echoes that arise from their round-trip time delay. In this example, there is a strong band of echoes near altitude(or range) index 25 with amplitudes that fluctuate in slow time.

Right) To resolve targets in velocity, FFTs are performed horizontally for each row in the data-matrix shown in step 2). The data-matrix shown on the right is referred to as the range-velocity matrix. The dimensions of the range-velocity matrix are $M/2$+1=129 rows by Q =256 columns. Hamming windows are applied in both stages of FFTs in order to reduce spectral leakage.

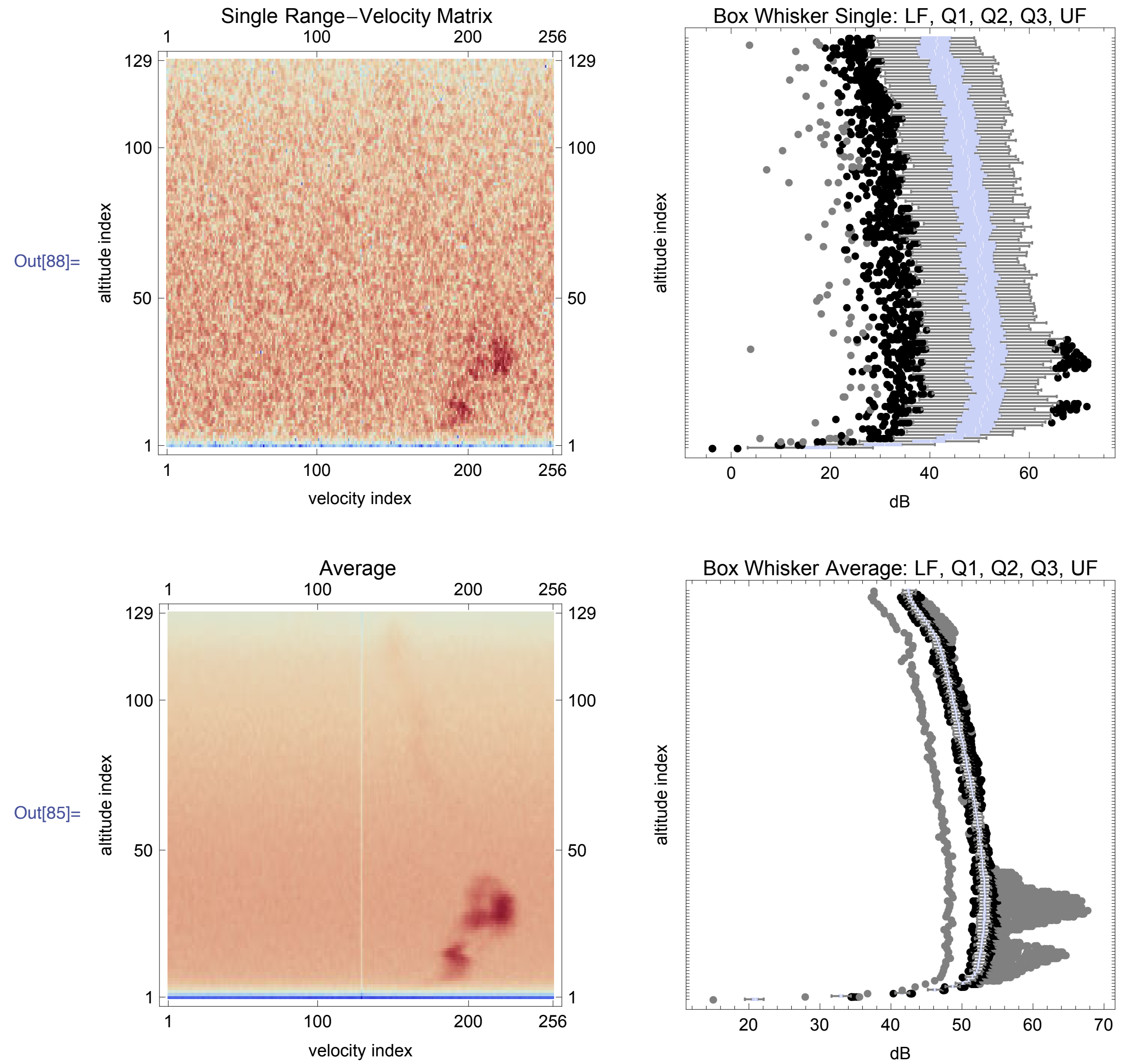

Spectral averages reduce fluctuations in the noise .

Echoes from strong reflectors are easily detectable in the range-velocity matrix but the weak reflections form clear air scatter and weather events require more processing gain. This is achieved by spectral averaging. The upper left image is a single range-velocity matrix and the lower image is the average of N_{avg}=171 range velocity matrices. This averaging is performed without overlap in order to maintain statistical independence. The lower left image is based upon about 11.5 sec of radar data. The degree to which the averaging process reduces background fluctuations is illustrated with the Box Whisker charts shown to the right. At each altitude step (row in the matrix) the Box Whisker chart depicts the statistics of the data at that altitude. Note the appearance of the weak echo extending from about altitude cell 75 out to cell 129. GW The background fluctuations in the single range-velocity matrix shown in the upper left completely obscure this weak echo. As of 2013 WiPPR data range velocity matrices were formed using 200 averages.

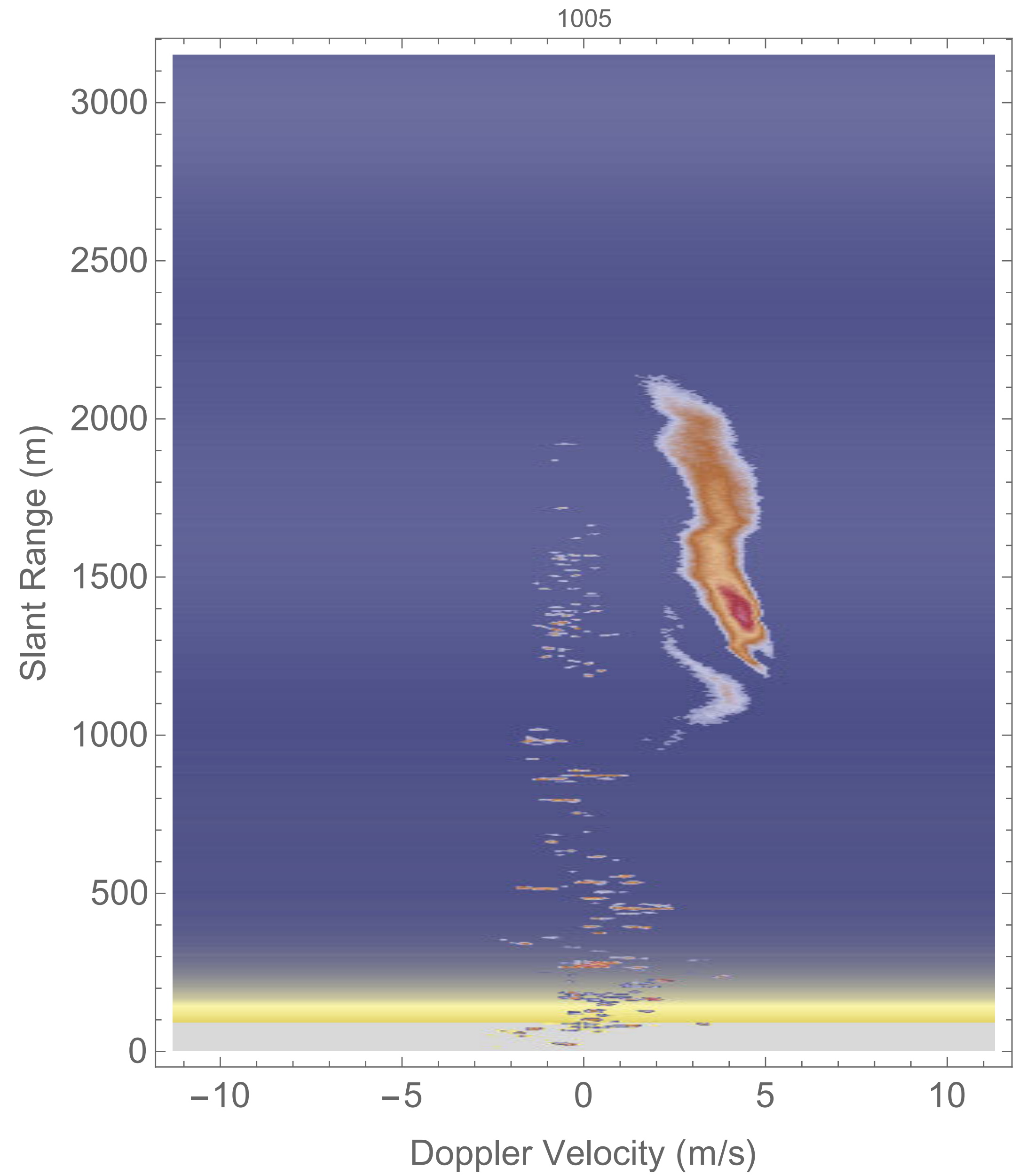

Range velocity matrix from 24 August 2017 at Stennis Airport, Hancock County, MS.

A range velocity matrix from a more recent version of the radar is shown above. The radar is detecting echoes from clear air scatter (convective turbulence) up to an altitude of about 2000 m. The radar is also detecting echoes from virga (two large blobs) which produce returns with a much smoother structure. The virga echoes appear at higher Doppler velocities because they are falling.

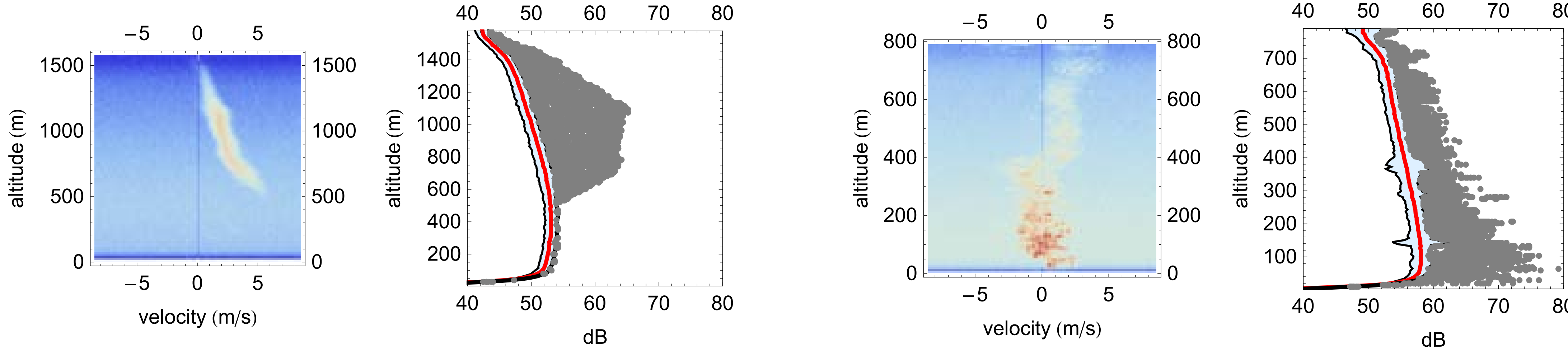

Left pair) Trace rainfall observed in Long Beach, MS on 8 November 2011. Right pair) High energy clear air scatter at Palm Canyon, AZ on 23 March 2012.

When we began the WiPPR project we thought that “clear air scatter” came from particles in the atmosphere that moved with the velocity of the wind. These particles could be hydrometers (rain, fog or hail), insects or dust. WiPPR actually see these types of targets quite well as shown by the upper left figure. We did not anticipate that WiPPR would be able to directly detect turbulence in the atmosphere in the absence of hydrometers, dust and insects. WiPPR has observed this turbulence at locations all over the continental US at altitudes up to 2000 meters. The strength of the turbulence is determined by atmospheric conditions, solar illumination as well as surface roughness. It is the defining characteristic of the convective boundary layer. Never before has it been seen with so much clarity and precision by a Ka band radar. The figure shown to the upper left shows an example of WiPPR detecting trace rainfall. This figure contains two parts 1) a range-velocity matrix and its 2) its associated box whisker chart. This is what we expected to see, including a smooth variation of contact density with altitude and velocity. The figure pair shown to the right shows an example of clear air scatter. The right hand figure pair is very typical of what WiPPR sees on a clear day. The echoes are much higher in amplitude than we anticipated and much more unevenly distributed in velocity. This necessitated the development of sophisticated velocity estimation techniques that could correctly deal with velocity outliers associated with high energy turbulent events. Additionally we thought that WiPPR performance would be governed by the weather radar equation. This implies that WiPPR range performance should increase with decreased FM sweep width and that WiPPR echoes should fall off inversely proportional to altitude squared. Both of these assumptions proved to be incorrect. The majority of the targets that WiPPR detects are point like and r^{-4} is the appropriate propagation model, not r^{-2}. If anything, radar performance is increased by using larger not smaller FM sweep widths.

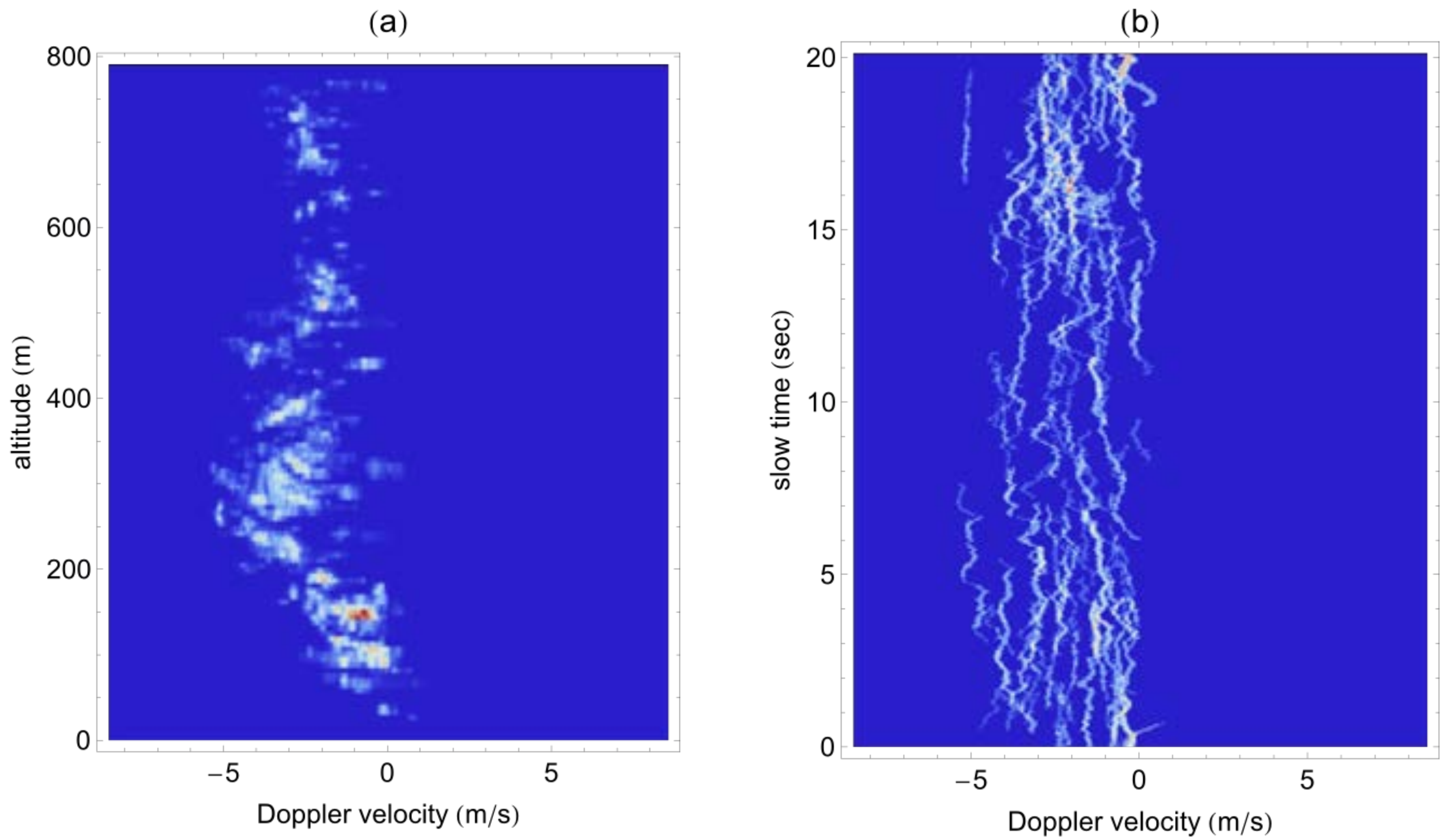

WiPPR measurement of Doppler velocity of the wind using data collected on 27 March 2012 at Yuma, AZ under absolutely clear skies.

WiPPR tracks the naturally occurring index of refraction anomalies produced by convective turbulence in and just above the convective boundary layer. This turbulence has a particle like character that produces radar cross sections that can be detected by the highly sensitive radar electronics. The fundamental quantities that an FMCW radar system measures are the distance, reflectivity and Doppler velocity of objects as they move through the radar beam as a function of time. This produces a 3 dimensional time-range-velocity radar data cube. The time span shown in the figure is 20 sec. If the radar data cube is averaged over time the result is the range velocity matrix (RVM) shown in a). If the data cube is thresholded in SNR and accumulated over altitude the result is the Doppler-time gram shown in b). RVMs are the measured quantity that is used to estimate wind velocity. The tracks moving through image (b) are caused by reflections from turbulence as it moves through the radar beam.

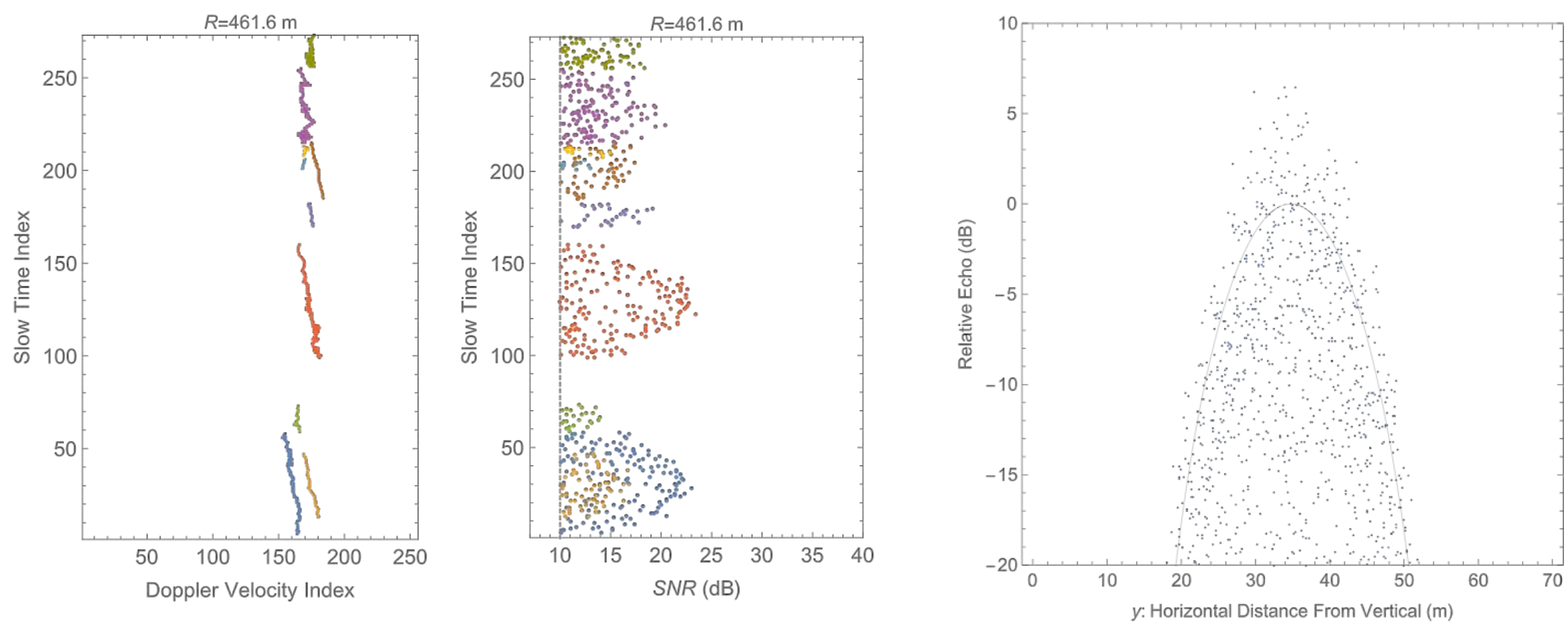

Left pair) Echoes from turbulent particles in WiPPR radar beam as a function of slow time. Right) Modeled echo response.

Left pair) Approximately nine turbulent particles are tracking through a WiPPR beam. Color is used to distinguish between particles. Notice the beam-pattern like character of the echo as a function of slow time. This implies that we are seeing point scatter as opposed to surface or volume scatter. Right) Radar echoes have been modeled. The model that is use here to represent radar echo is two-way radar beam response on a power scale times a random sample from a gamma distribution. The radar antenna is modeled as a circular aperture with radius a where the value of a has been chosen to produce the appropriate amount of directivity. Specifically we use is

$$B(\theta) = [2J_1(ka\sin(\theta)/ka\sin(\theta)]^4$$

where θ is the angle of the particle position with respect to the radar beam axis. The probability density function of the gamma distribution is

$$p(x\,|\,\alpha,\sigma) = \Gamma(\alpha)^{-1}\sigma^{-1}(x/\sigma)^{\alpha-1}\exp(-x/\sigma)$$

where x is a realization of the radar cross section of the target. The parameters α and σ have been chosen by eye to be respectively 0.5 and 1.

Wind Velocity Inversion

Wind velocity inversion is the process through which the wind velocity profile $(v_x(z), v_y(z), v_z(z))$ at altitudes z is estimated from scalar Doppler velocity measurements made on WiPPR radar beams pointed in the cardinal directions (N, E, S, W). If all scattering objects were moving horizontally then sophisticated procedures would not be required to determine wind velocity from Doppler velocity. But this is not the case. Falling hydrometers and updrafts are common in the convective boundary layer.

WiPPR employs four, near vertical beams to address the falling object problem. Specifically these beams are pointed in the directions

$$\overrightarrow{\eta} = (\cos(\theta)\sin(\phi), \cos(\theta)\cos(\phi, \sin(\theta))$$

where θ is the beam elevation angle and $\phi = 0, \pi/2, \pi, \ 3\pi/2$ is a rotation angle measured in the horizontal plane with respect to north. Beams 1-4 point in the directions N, E, S and W as shown in a following figure.

The relationship between the wind velocity $\overrightarrow{v} = (v_x, v_y, v_z)$ at an altitude and the Doppler velocity V measured at that altitude for the beam with angular pointing direction (ϕ, θ) is

$$V = -\overrightarrow{\eta} \,.\, \overrightarrow{v}$$

If (V_1, V_2, V_3, V_4) denote the Doppler measurements at an altitude then

$$V_1 = -\cos(\theta)v_y - \sin(\theta)v_z, \; V_2 = -\cos(\theta)v_x - \sin(\theta)v_z,$$

$$V_3 = +\cos(\theta)v_y - \sin(\theta)v_z, \; V_4 = +\cos(\theta)v_x - \sin(\theta)v_z$$

Simple linear algebra or the principle of least squares implies that the corresponding wind velocity is

$$v_x = \frac{1}{2\cos(\theta)}(V_4 - V_2), \;\; v_y = \frac{1}{2\cos(\theta)}(V_3 - V_1)$$

and

$$v_z = -\frac{1}{4\sin(\theta)}(V_1 + V_2 + V_3 + V_4)$$

The conventions that we employ is here $v_x > 0$ at an altitude means that the wind has a velocity component at that altitude that is coming from the West. If $v_y > 0$ then the wind has a component that is coming from the South. If $v_z > 0$ then the wind has a vector component that is coming from below. If the Doppler velocity V is positive at an altitude then the object producing that echo is moving towards the radar.

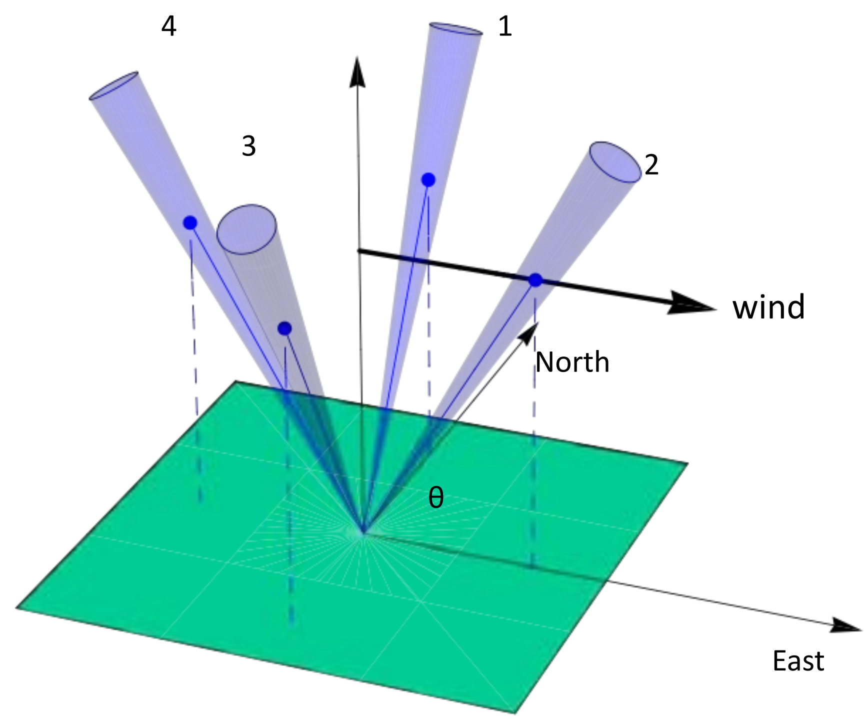

In the special case $v_z = 0$, the solutions for (v_x, v_y, v_z) in terms of (V_1, V_2, V_3, V_4) have simple physical interpretations. Consider beam 3 and the wind velocity component v_y with $v_y > 0$. Consider an object moving with the wind. The Doppler measurement will be $V_3 = \cos(\theta)v_y$. If beam 1 sees this same object then we will have $V_1 = -\cos(\theta)v_y$. Thus provided $v_z = 0$

$$v_y = V_3/\cos(\theta) = -V_1/\cos(\theta).$$

and similarly

$$v_x = V_4/\cos(\theta) = -V_2/\cos(\theta)$$

WiPPR uses an elevation angle of $\theta = 80$ deg. This produces an unambiguous wind velocity range of

$$\left(-\frac{c}{4T_m f_c \cos(\theta)}, \frac{c}{4T_m f_c \cos(\theta)}\right) = (-68.1, 68.1)\ \text{m/s}$$

In general data from more than 4 range velocity matrices will be combined to estimate a wind velocity at an altitude. Suppose we have D measurements of Doppler

$$\mathbf{V}_{obs} = (V_1, V_2, \ldots, V_D)^T$$

each made at radar beams pointing in the directions

$$\vec{\eta}_d = (\cos(\theta)\sin(\phi_d), \cos(\theta)\cos(\phi_d), \sin(\theta))$$

where $d = 12,\ldots,D$ and the ϕ_d take on one of the azimuthal pointing directions $(0,\pi/2,\pi,3\pi/2)$. The relationship between the vector of observed Doppler values and the wind velocity vector can be written in matrix notation as

$$\mathbf{V}_{obs} = -\,\mathbf{A}\,.\,\mathbf{v}$$

where $\mathbf{A}$ is the matrix of beam pointing directions and $\mathbf{v} = (v_x, v_y, v_z)^T$ is the wind velocity vector. It we define $\mathbf{B} = -\,\mathbf{A}$ then

$$\mathbf{V}_{obs} = \mathbf{B}\,.\,\mathbf{v}$$

If the Doppler data $\mathbf{V}_{obs}$ are measured with Gaussian errors characterized by the standard deviation σ_V, then the likelihood of $L(v_x, v_y, v_z \,|\, \mathbf{V}_{obs})$ of observing these data is

$$L = (2\pi)^{-D/2}\sigma_V^{-D}\Pi_{d=1}^{D}\exp[-\frac{1}{2\sigma_V^2}(V_d - \mathbf{v}\,.\,\vec{\eta}_d)^2]$$

This likelihood can be written in the matrix form

$$(2\pi)^{-D/2}\sigma_V^{-D}\exp[-\frac{1}{2\sigma_V^2}(\mathbf{V}_{obs} - \mathbf{B}\,.\,\mathbf{v})^T\,.\,(\mathbf{V}_{obs} - \mathbf{B}\,.\,\mathbf{v})]$$

The value of $\mathbf{v}$ which maximizes this likelihood is the least square solution

$$\mathbf{v}_{LS} = (\mathbf{B}^T\,.\,\mathbf{B})^{-1}\,.\,\mathbf{B}^T\,.\,\mathbf{V}_{obs}$$

This matrix equation yields a solution provided that the Doppler data at the altitude includes at least 3 of the 4 beam pointing directions.

The least square approach has been the primary velocity inversion procedure used by WiPPR since the beginning of the project. Typically we allow the radar to revolve 3 times and acquire 12 beams of data. Wind velocity estimates are made at each altitude where there is data on at least 3 distinct beams. Linear interpolation is used to fill in the gaps.

The likelihood of the data $L(v_x, v_y, v_z \,|\, \mathbf{V}_{obs})$ can also be written in the form (apart from a factor of $(2\pi)^{-D/2}$)

$$\sigma_V^{-D} \exp[-\frac{RSS}{2\sigma_V^2}] \exp[-\frac{(\mathbf{v} - \mathbf{v}_{LS})^T . \mathbf{B}^T . \mathbf{B} . (\mathbf{v} - \mathbf{v}_{LS})}{2\sigma_V^2}]$$

where

$$RSS = (\mathbf{V}_{obs} - \mathbf{B} . \mathbf{v}_{LS})^T . (\mathbf{V}_{obs} - \mathbf{B} . \mathbf{v}_{LS})$$

is the residual sum of squares. The matrix

$$\mathbf{F}_{Fisher} = \sigma_V^{-2} \mathbf{B}^T . \mathbf{B}$$

is the Fisher information (or precision) matrix of the measurement. Large Doppler measurement errors make for low precision. The inverse of the Fisher information matrix is the covariance matrix

$$\mathbf{\Sigma} = \sigma_V^2 (\mathbf{B}^T . \mathbf{B})^{-1}$$

The covariance matrix represents the error with which we estimate the velocity . The square roots of the three diagonal elements of the covariance matrix are the standard deviations associated with the least squares estimate of the wind velocity.

In most circumstances we do not know the Doppler measurement error σ_V. An estimate of its value is

$$\sigma_V^2 = \frac{1}{D-3} RSS$$

In the above equation we divide by $D - 3$ because three parameters (v_x, v_y, v_z) have been estimated from the data.

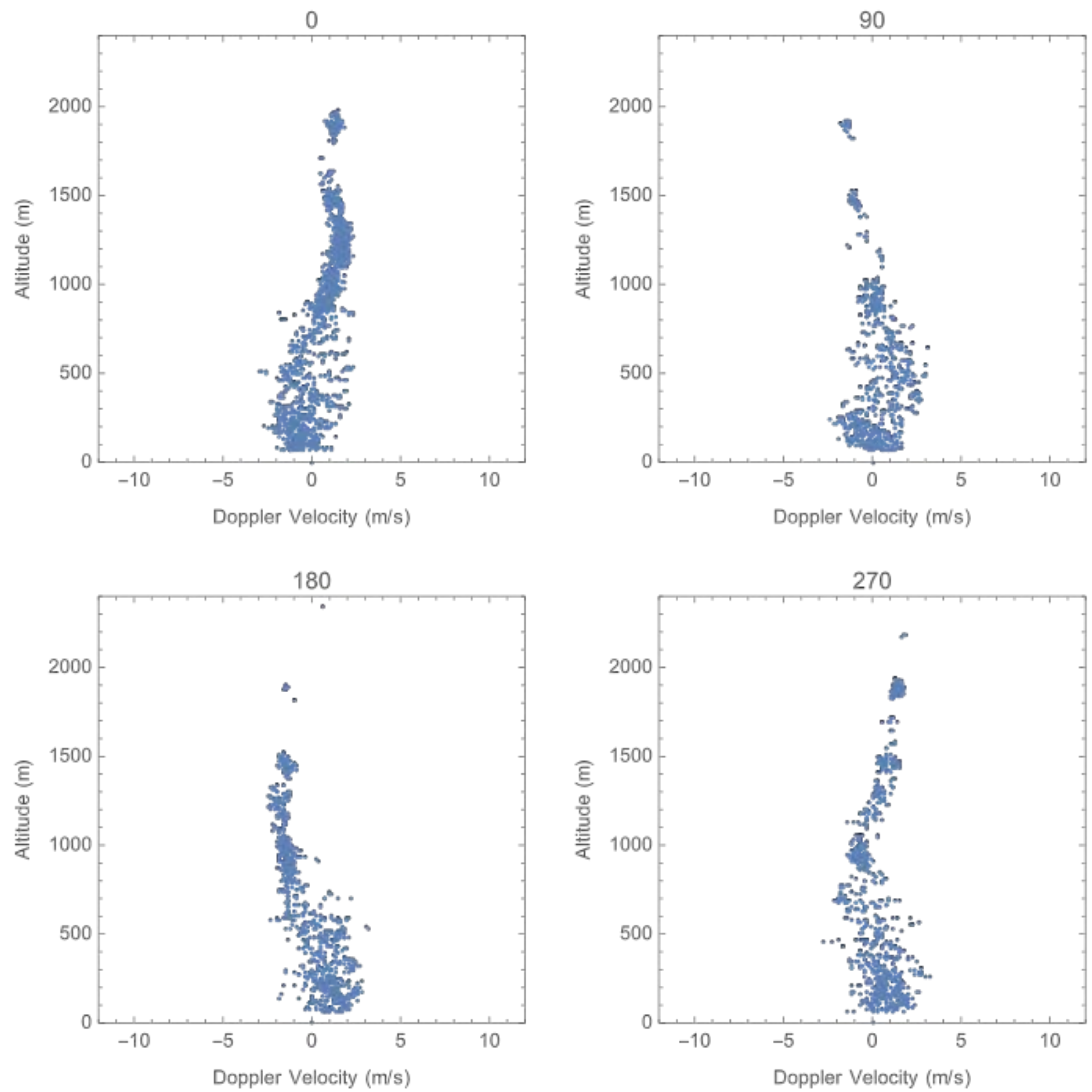

WiPPR Doppler data from 26 June 2017 at Yuma, AZ.

Doppler data was recorded on 4 beams. Beams 1-4 are respectively pointed in the directions 1) north (0 deg), 2) east (90 deg), 3) south (180 deg) and 4) west (270 deg). The beams are nearly vertical with each beam elevated 80 deg from the horizontal (10 deg off vertical). The radar echoes are from heat generated turbulence that has floated up to the top of the convective boundary layer. Beam 3 directly measures the the v_y component of wind velocity within the scale factor $1/\cos(80\text{ deg})$. Beam 4 directly measures the v_x component of wind velocity within this scale factor. Note the 180 deg left-right symmetry in the data between beam 1 and 3 and also beams 2 and 4. This provides a strong indication that the WiPPR system was correctly functioning. The figure was produced from 21 total data files, each 18 sec apart.

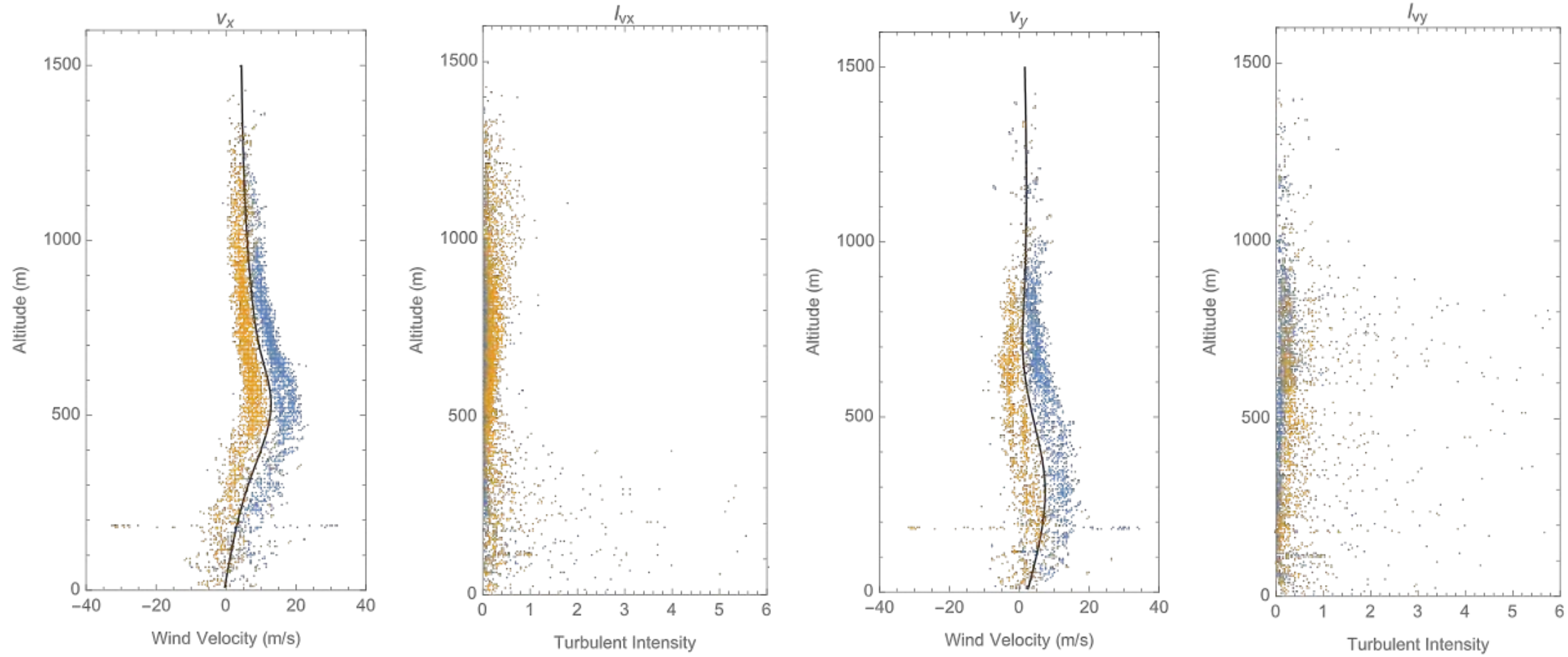

Instantaneous and average wind velocity products.

The WiPPR system makes instantaneous measurements of Doppler velocity on 4 radar beams (1-4) that sequentially point in the directions N, E, S and W. If the radar is detecting reflections from objects that are not falling then wind velocity can be determined a very simple procedure. The simple wind velocity estimates are computed by dividing each beam's Doppler data by cosθ where θ is the beam elevation angle and multiplying by -1 on beams 1 and 2. This last steps accounts for the fact that beam1 and and 3 as well as 2 and 4 respectively point in opposite directions. Wind moving from S to N is observed as positive Doppler on 3 and negative Doppler on beam 1. The dots in the above figure are instantaneous measurements. Color is used to indicate beam number. Darker color is lower beam number. Also shown are instantaneous estimates of turbulent intensity, a quantity which is significant in wind pressure loading. The solid black lines are WiPPR wind velocity estimates using a global cubic spline model developed for airborne operations and later adapted to ground-based radar applications.

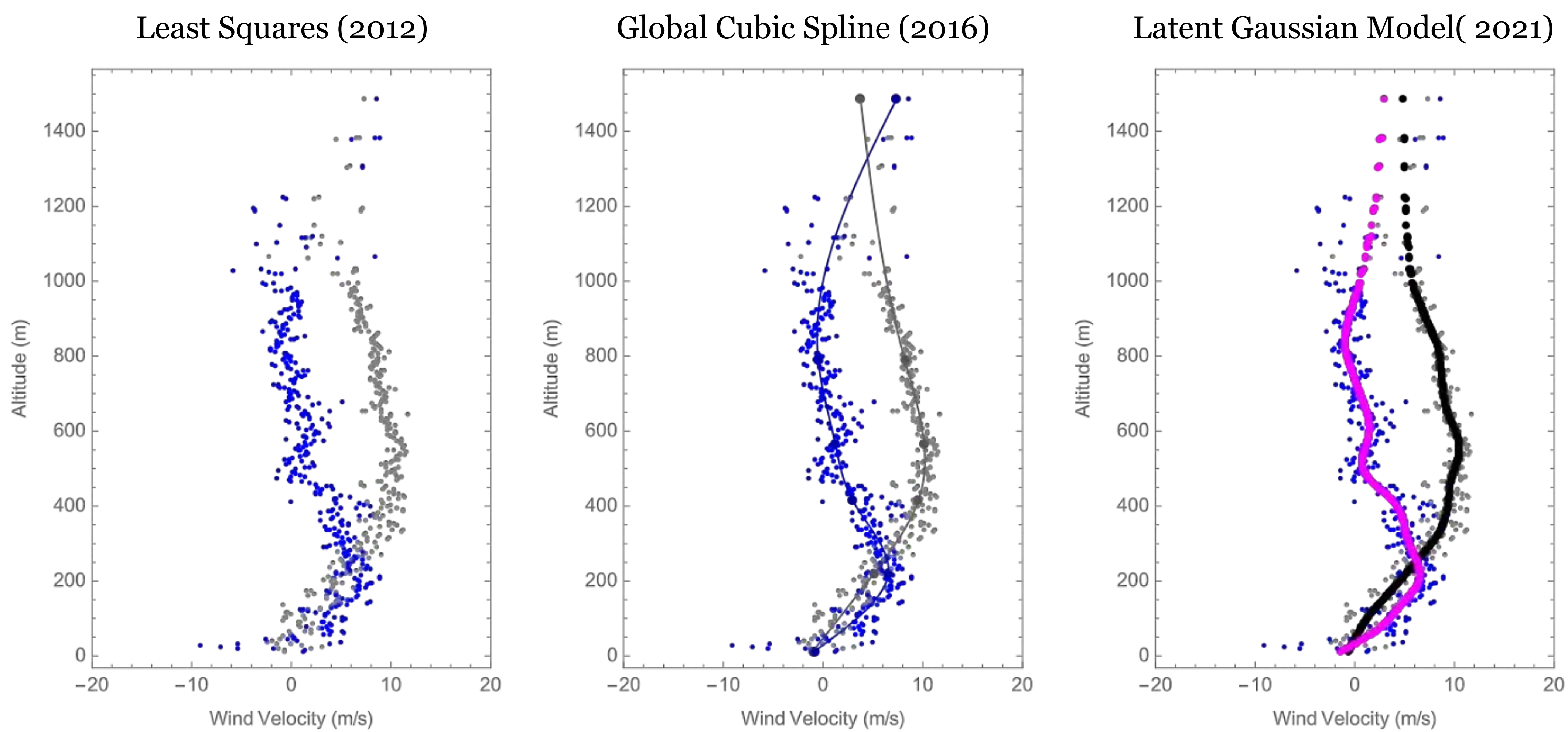

Comparison of wind velocity inversion procedures 2012-2021.

The above figure shows wind velocity profile estimates using the three primary wind velocity inversion techniques developed during 2012-2021. (Left) Wind velocity inversion using the least squares technique described in this document. (Center) Estimates using the global cubic spline technique developed for airborne operations. (Right) Wind velocity estimates using a Latent Gaussian Model (LGM) approach popularized by the statistician Harvard Rue. The LGM approach shows great promise for applications where the fine structure in the wind speed profile is important. The LGM approach imposes sensible spatial structure on the wind speed profile without over smoothing. Unknown parameters in the LGM model are found by maximizing the Bayesian evidence.

Validation of WiPPR Concept

Validation in the context of WiPPR refers to two complimentary points. WiPPR obtains wind velocity estimates as a function of altitude by primarily observing echoes from clear air scatter. We now know that this is mainly heat-generated convective turbulence that has a point like reflective character. The radar can track and make velocity estimate from this turbulence. The radar can also make these velocity estimates from echos from rain, virga, fog and snow. So a very fundamental question is the following: Is convective turbulence with sufficient echo producing intensity widely distributed enough spatially and seasonally to support a practical system that works under clear skies. A second question is as follows: Given the presence of convective turbulence in the atmosphere (or rain or snow) can the radar produce wind velocity estimates that agree with other trusted wind sensing devises. Specifically we mean ground launched (or air dropped) radio sondes that compute wind velocity through the use of GPS tracking technology. These are considered the gold standard.

From the onset of the WiPPR program in 2010 we had access to QNA balloon lifted radio sondes. Over the next seven years we launched approximately 80 of these sondes and made numerous successful comparisons of WiPPR measurements to sonde measurements of wind velocity. We also had access to radio sonde data from the Slidell, LA airport. This airport was close enough to our engineering offices in Waveland, MS that we could use it for comparison purposes as well. The results were very favorable.

Beginning in January 2015 we conducted a nation-wide measurement program to confirm the spatial and seasonal repeatability of the atmospheric phenomena that WiPPR exploits to measure wind velocity. The results were very favorable. We were able to successfully measure wind speed profiles at Yuma AZ, Dugway UT, Lawerence Livermore CA, Edwards AFB CA, Wright Patterson AFB OH, Stennis Airport MS, Boulder CO, Rome NY and Charleston SC in both winter and summer conditions. Additional wind measurements were successfully made at Eloy AZ, Locke Station MS, Waveland MS.

The only situation where WiPPR encountered difficulty was on snowy ground and cold high pressure atmospheric conditions. This reduced target contact rates but it was still possible to produce wind profiles by accumulating data over long time intervals (hours instead of minutes).

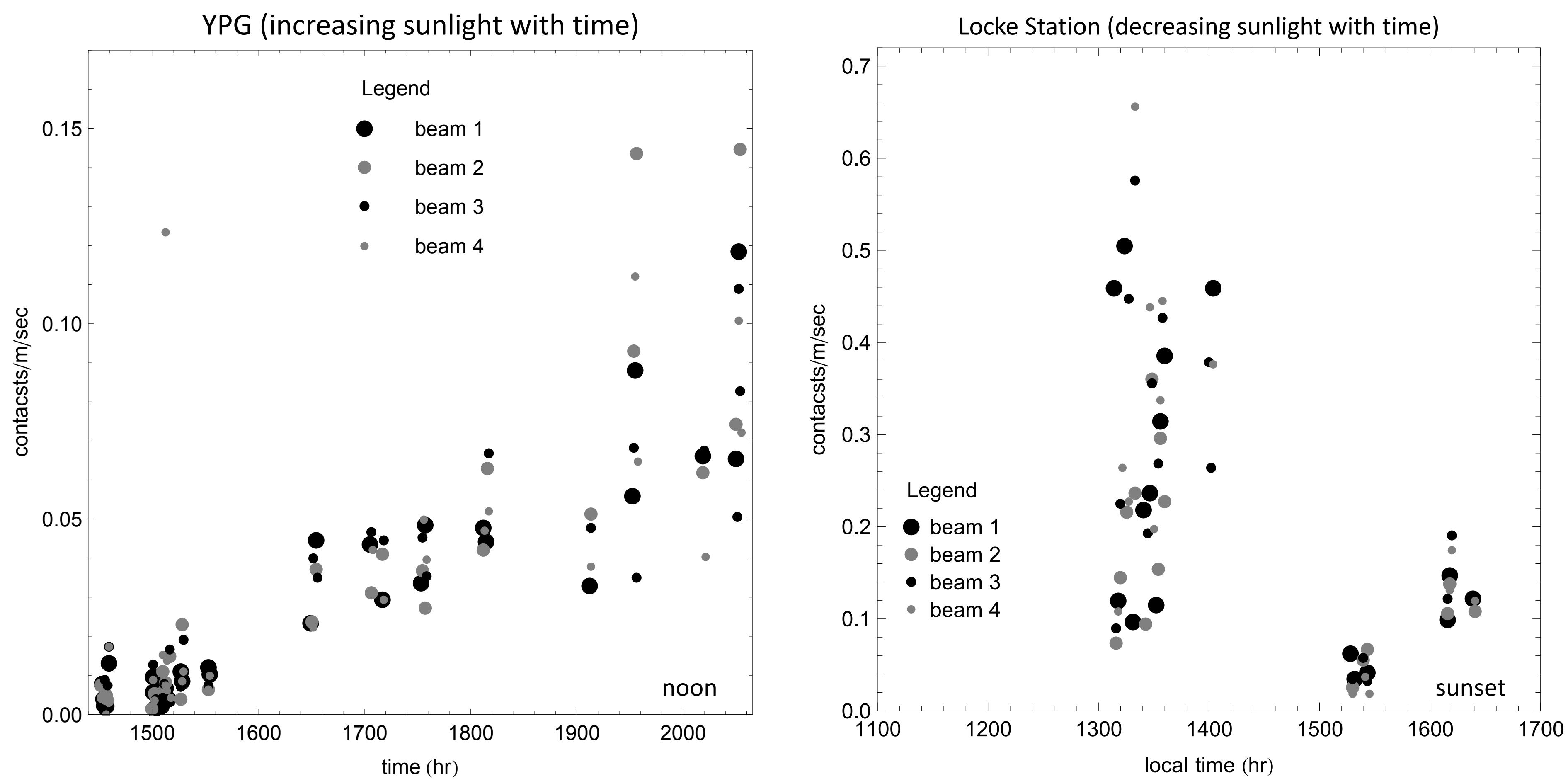

Variation of clear air scatter contact density with solar illumination 2011 and 2012.

By March 2012 we strongly suspected that clear air scatter was sun-generated convective turbulence and not insects. The figure above compares WiPPR contact density as a function of time during periods of increasing sunlight (YPG, March 2012) and decreasing sunlight (Locke Station, MS, December 2011). The Locke station measurements were made in winter and there were no insects. Note the vertical scale change between the data sets due in part to the change in sweep width The YPG data were collected with a 24 MHz sweep width. The Locke Station data was recorded with a 48 MHz sweep width. Both days were crystal clear with unlimited visibility. Contact densities are significantly higher at the 48 MHz sweep width (Locke Station) than for the 24 MHz sweep width (YPG). In both locations contact density is obviously influenced by the rise and fall of the sun.

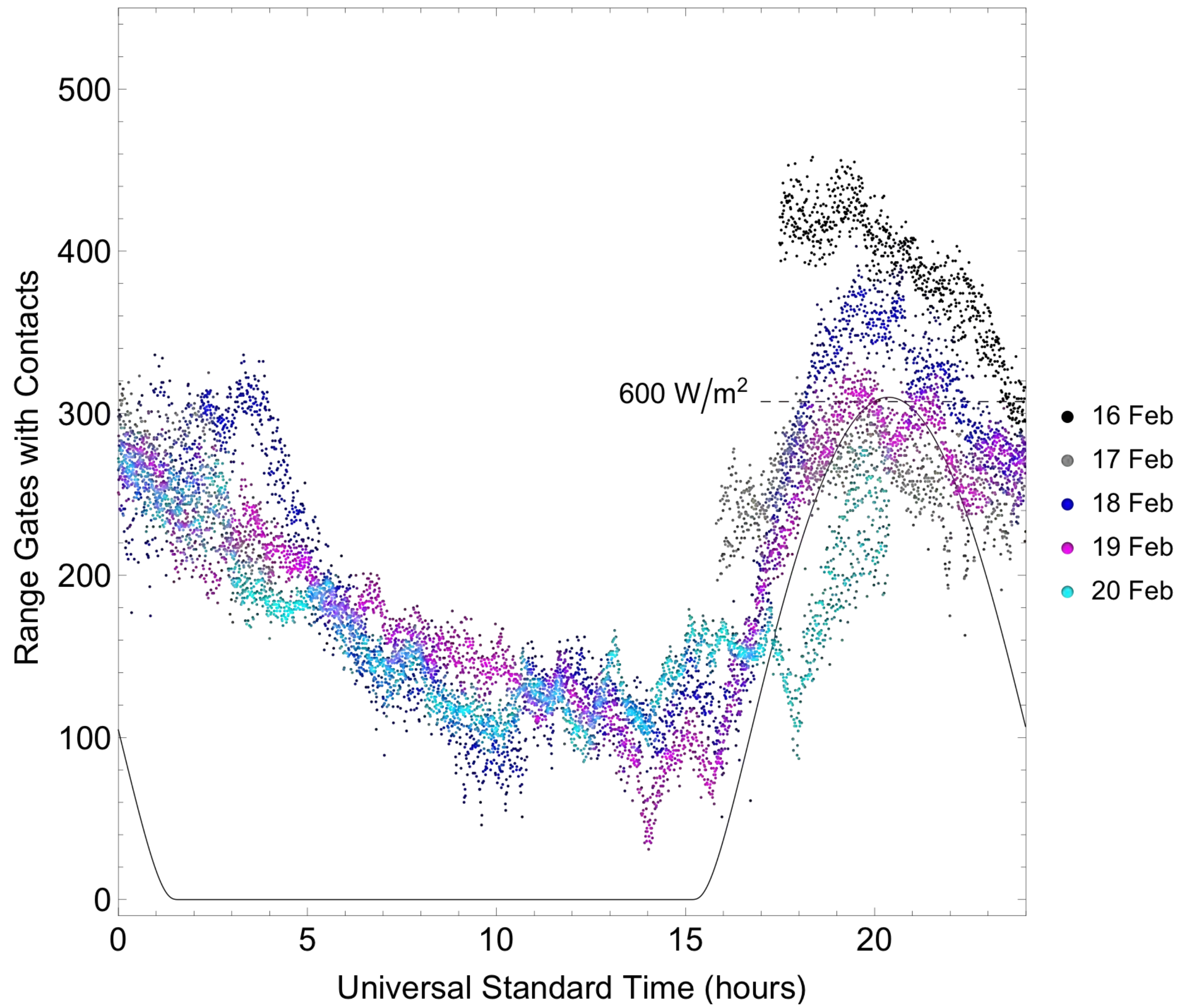

Effect of solar illumination on radar contact rate using radar data from Lawrence Livermore 15-20 February 2015.

By the end of February 2015 we knew clear air scatter was heat generated turbulence. In the above solar illumination is indicated by the solid black line. Solar noon on 18 February 2015 occurs at 20.37 hrs UST. Radar contact rates are consistently highest at noon and lowest just before dawn. A radar contact is a Doppler echo in a range-velocity cell with a post processing SNR greater than 2 dB. The solar illumination curve is adapted from the book *Meteorology for Scientists and Engineers* (2nd ed) by Roland B. Stull. At local noon anywhere from 300 to 450 range gates have contacts. The radar cell widths are 3.125 in extent. Thus at this time the radar is detecting echos from the turbulence at slant ranges of 1000-1350 meters. Between 0 and 1500 UST the convective boundary layer collapses and forms the night residual boundary layer.

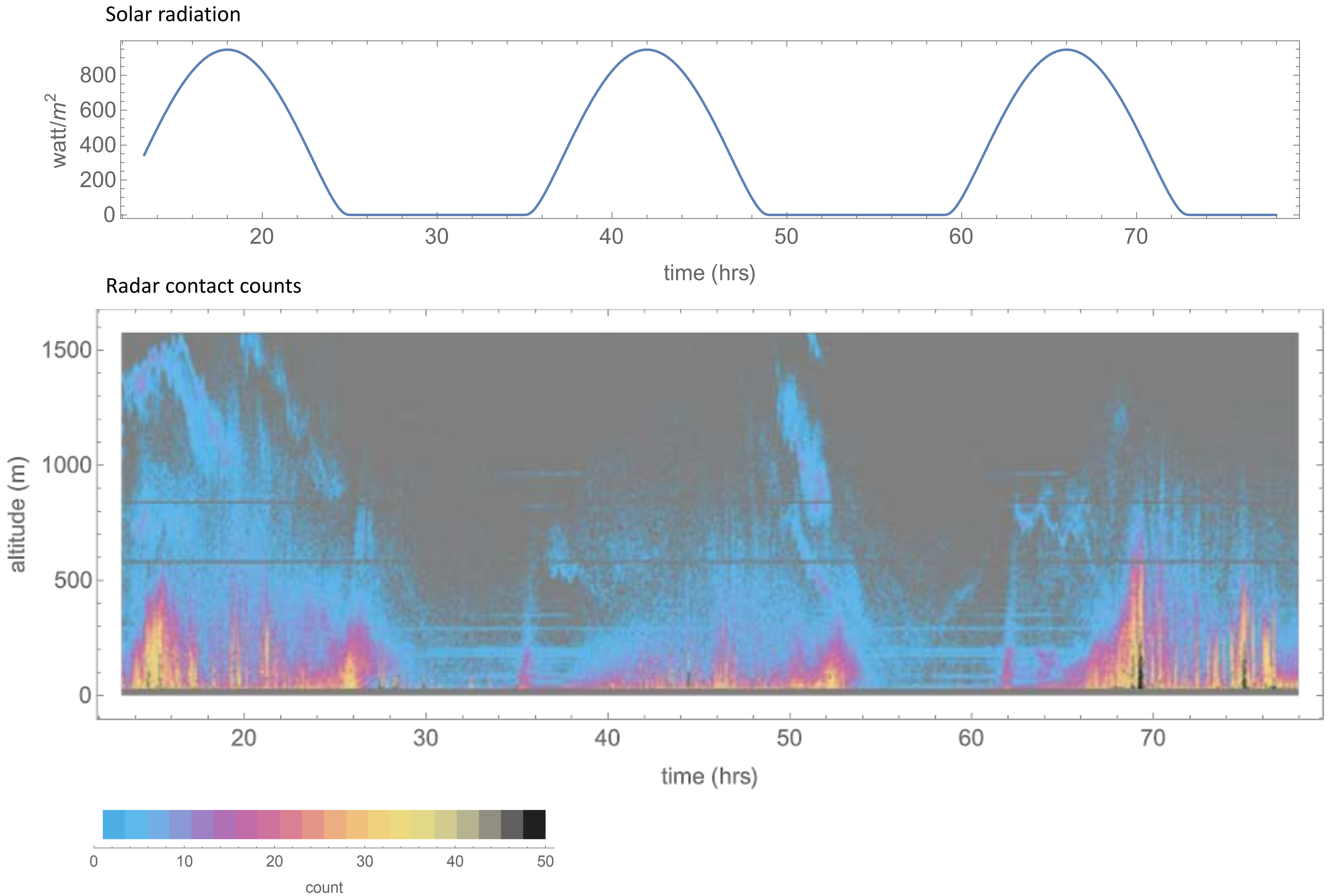

Solar radiation vs radar contacts: Rome NY July 2015

The above figure shows variation of radar contacts with solar illumination over a 3-day times period. Contact rates increase with increasing solar illumination and fall off in the late afternoon when the sun sets. There is a residual boundary layer at night. These data were recorded during a period of clear skies. Background color gray indicates zero contacts. The horizontal lines are processing artifacts.

WiPPR radar system with 31 dB gain antennas in December 2012 at Waveland, MS.

Numerous test measurements were made with this version of WiPPR at our offices in (at that time) Waveland, MS during the April-December 2012 time frame. Waveland is near the Slidell, LA airport where radiosondes are launched at 6 AM and 6 PM every day. This data is readily accessible and made for easy comparisons between WiPPR wind measurements and sonde wind measurements. The ground is very flat on the Mississippi-Louisiana Gulf Coast and winds are almost always the same at both locations unless a front is passing through.

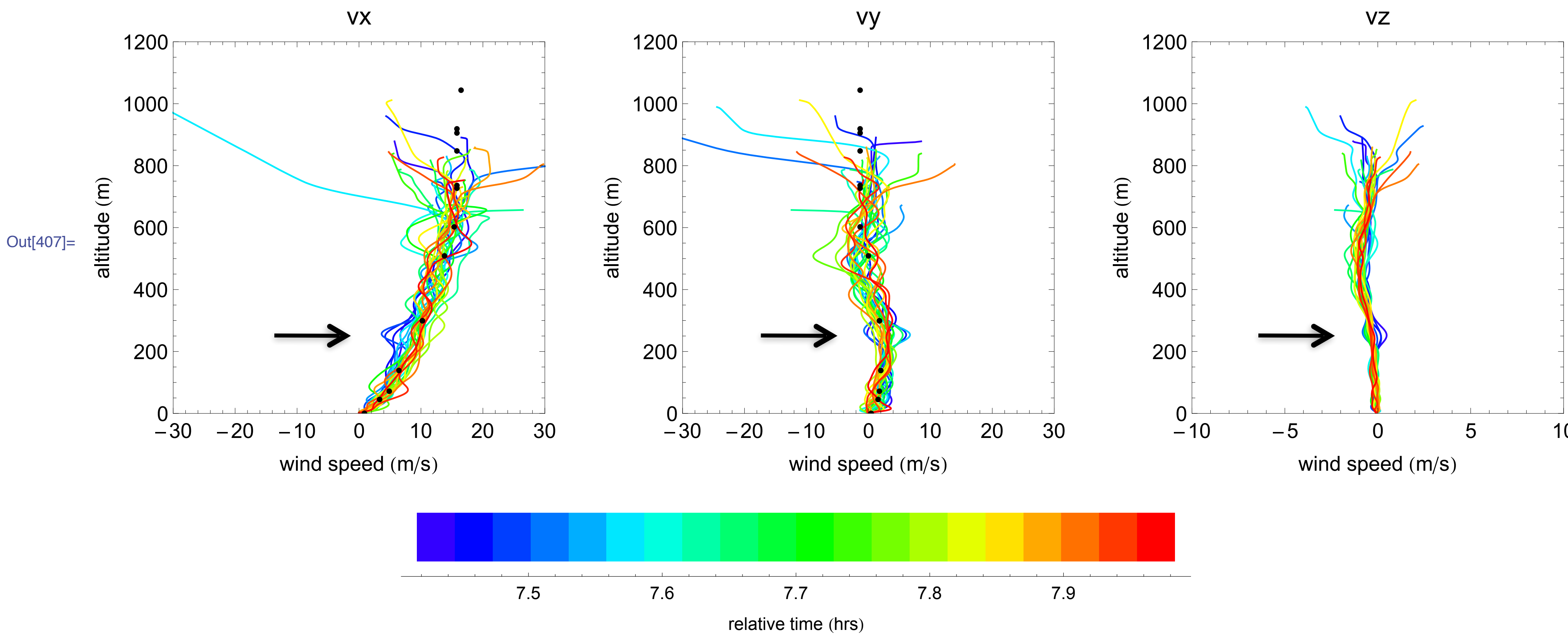

WiPPR Waveland Mississippi 17 December 2012 compared to Slidell radiosonde.

The above figure shows 27 GWPPR wind sticks measured on the afternoon of 17 December 2012 in Waveland, MS over a 32 minute time period. Skies in Waveland were clear. This was the first time that GWPPR with the new data acquisition system had been operated in a full-up configuration. Radiosonde ground truth data from the afternoon launch at the Slidell, LA airport is shown via the black dots. The black arrow indicates velocity artifacts due to system noise. There is clearly a GWPPR "walk-about" problem at the top of some of the wind sticks, especially with the wind stick recorded at about relative time 7.6 (very light blue trace). Apart from this relatively minor and correctable problem, the agreement between the GWPPR measurements over a one-half hour time period and the Slidell balloon data is very good. Radio sondes do not measure vertical wind velocity.

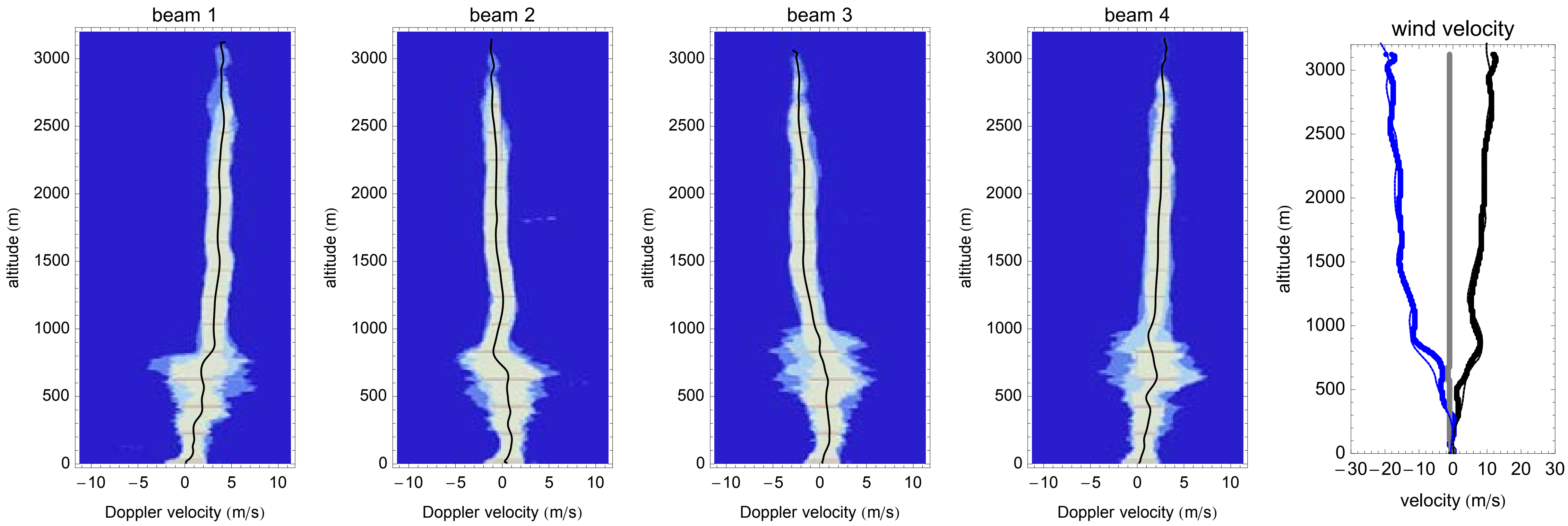

WiPPR 29 January 2013 at Dugway Utah compared to 1808 balloon launch

In January 2013 WiPPR traveled to Dugway, UT to participate in an experiment with a group of LIDAR systems. The above data were measured during a period of light snow. Radar wind speeds are compared to sonde wind speeds in the right most figure. The thick black, blue and gray blinds are the radar measurement of the (v_x, v_y, v_z) wind speed profiles. The thin black and blue lines are the corresponding sonde measurements. The agreement is almost exact. The left most four figures are cumulative range velocity matrices measured by the radar on beams 1-4 (N, E, S and W). The black lines are the projection of the wind velocity obtained by the radar back onto Doppler velocity space. The LIDARS that participated in the experiment were nonfunctional during this time period due to backscatter overload. WiPPR worked perfectly.

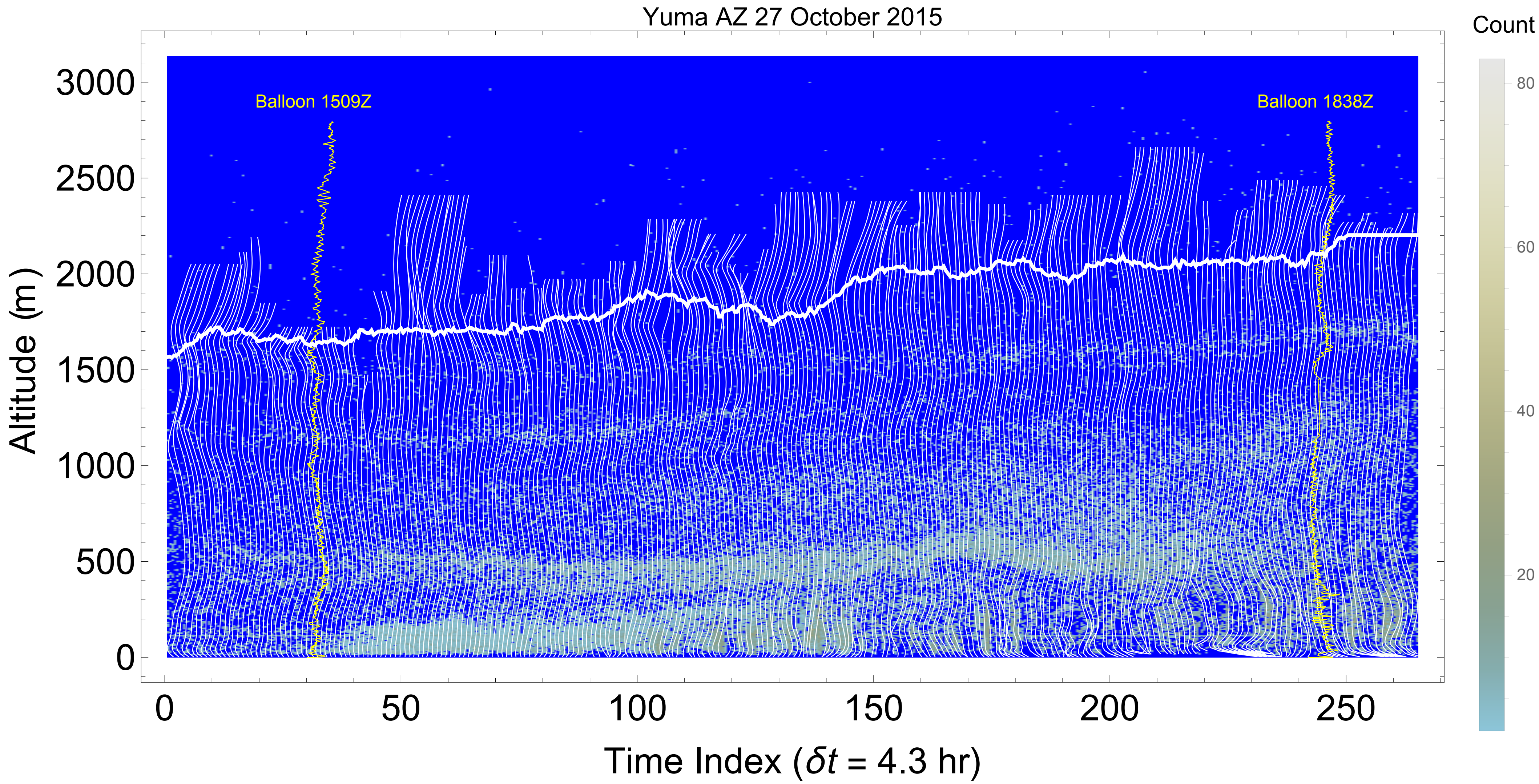

Wind speeds observed by WiPPR on 27 October 2015 at Yuma, AZ compared to radiosondes.

On 27 October 2015 a total of 552 range velocity matrices (RVM) were recorded by WiPPR over a 4 hour and 18 minute time period (δt=4.3 hr). Conditions were clear. These RVMs have been used to produce 521 wind velocity profiles using a partition size of 32 with an overlap of 31 RVMs. This is the absolute finest temporal grid that the measured data will support. The background in the above figure is the contact gram for the 27th. The top of the boundary layer has been estimated using a change detection algorithm and is shown as a thick white line. In addition to radar measurements, two QNA balloons were launched on the 27th and wind speeds from these balloons are shown in yellow. Due to the high density of the measured WiPPR wind profiles, only every other one has been plotted.

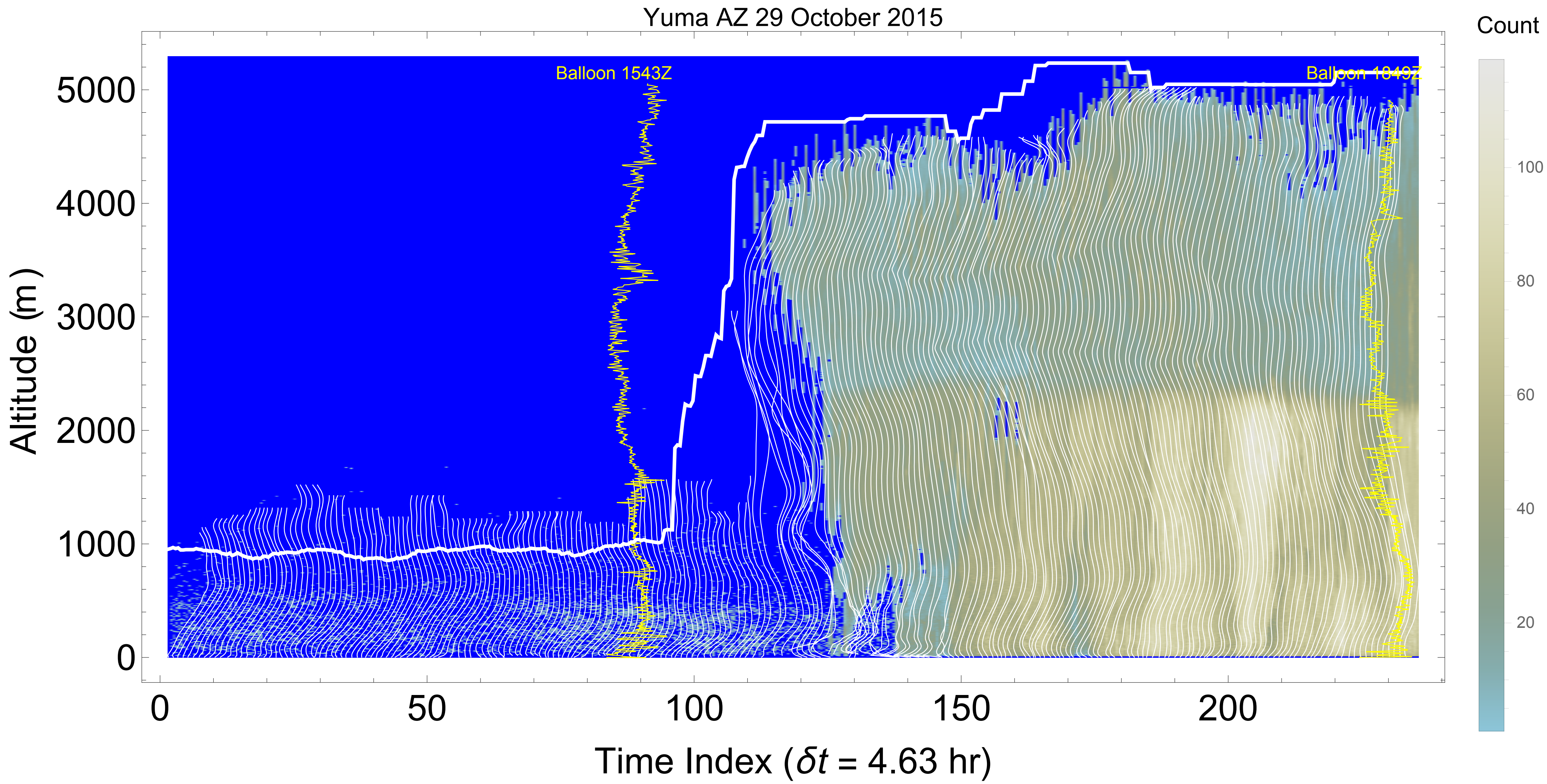

Wind speeds observed by WiPPR on 29 October 2015 at Yuma, AZ compared to radiosondes.

There are a total of 456 speed profiles in the figure shown above.   Format is similar to the previous figure. It began to rain about midway through the measurement. This cause a rapid increase in radar ceiling.

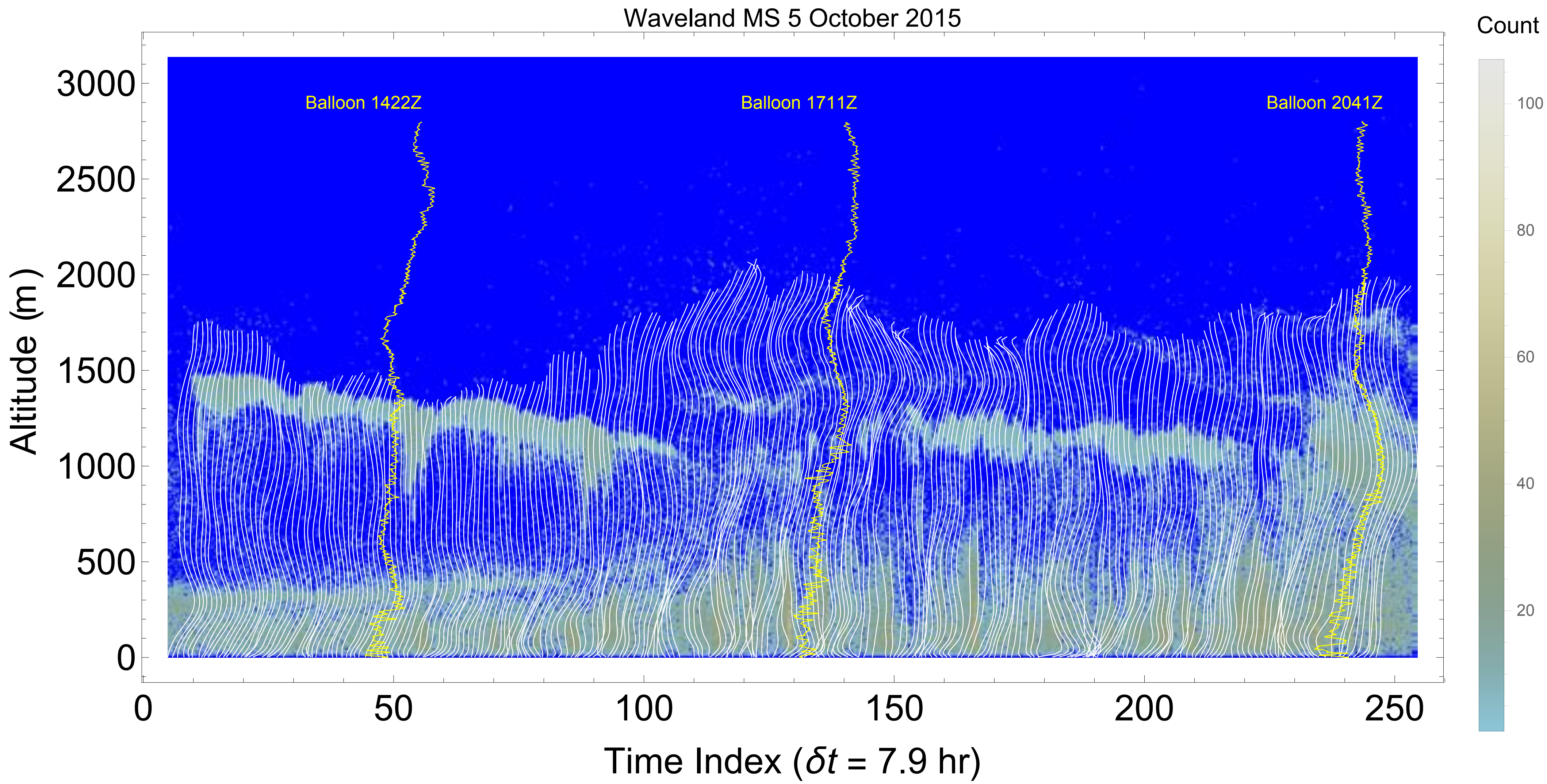

Wind speeds observed by WPPR on 5 October 2015 at Waveland, MS compared to radiosondes.

Atmospheric Phenomena Observed by WiPPR

In reviewing WiPPR data from June 2017 at Yuma, AZ it was observed that the WiPPR system detected a variety of atmospheric phenomena that we found to be interesting. We believe that the WiPPR system's ability to detect and characterize these phenomena may be interesting to scientists interested in atmospheric boundary layer physics. The phenomena that we focus on here are nocturnal jets, midday gravity waves and the Ekman spiral of wind direction in a neutrally stable atmosphere. Examples of virga (rain that does not reach the ground) have been previously shown in this document.

In this section we will primarily focus on what the radar sees instantaneously, i.e in individual range velocity matrices. Historically the focus in WiPPR has been on the production of average wind velocity profiles in support of precision air drop of parachute delivered supplies. We have gone to great lengths to build wind profiles that go as high as possible. We accumulate data over many minutes in order to obtain contacts from clear air scatter and use integration techniques to build a wind profile that goes up to the highest possible altitude in a sensible fashion. The tool that we ultimately chose for doing this was the natural cubic spline. It worked great for the intended application. However in building the wind profiles using the spline we have thrown away information that is useful to other potential users.

Nocturnal jets are anomalously high winds that occur several hundred meters above the ground at night, typically under clear sky conditions. Peak speeds may be in excess of the driving geostrophic winds that occur at much high altitudes. Sometimes nocturnal jets are described as being super geostrophic. Nocturnal jets are a complicated function of a variety of factors including density effects, terrain topography, radiative cooling in the air and surface cooling rates.

Gravity waves in the atmosphere are similar to ocean surface waves in that the restoring force is gravity. However they exhibit a much more complicated structure with elevation and time due to the thermal and hydrodynamic complexities of the convective boundary layer. We have routinely observed gravity waves in daylight hours in the desert. The result is a wind profile that fluctuates rapidly with time and altitude.

Nocturnal Jets

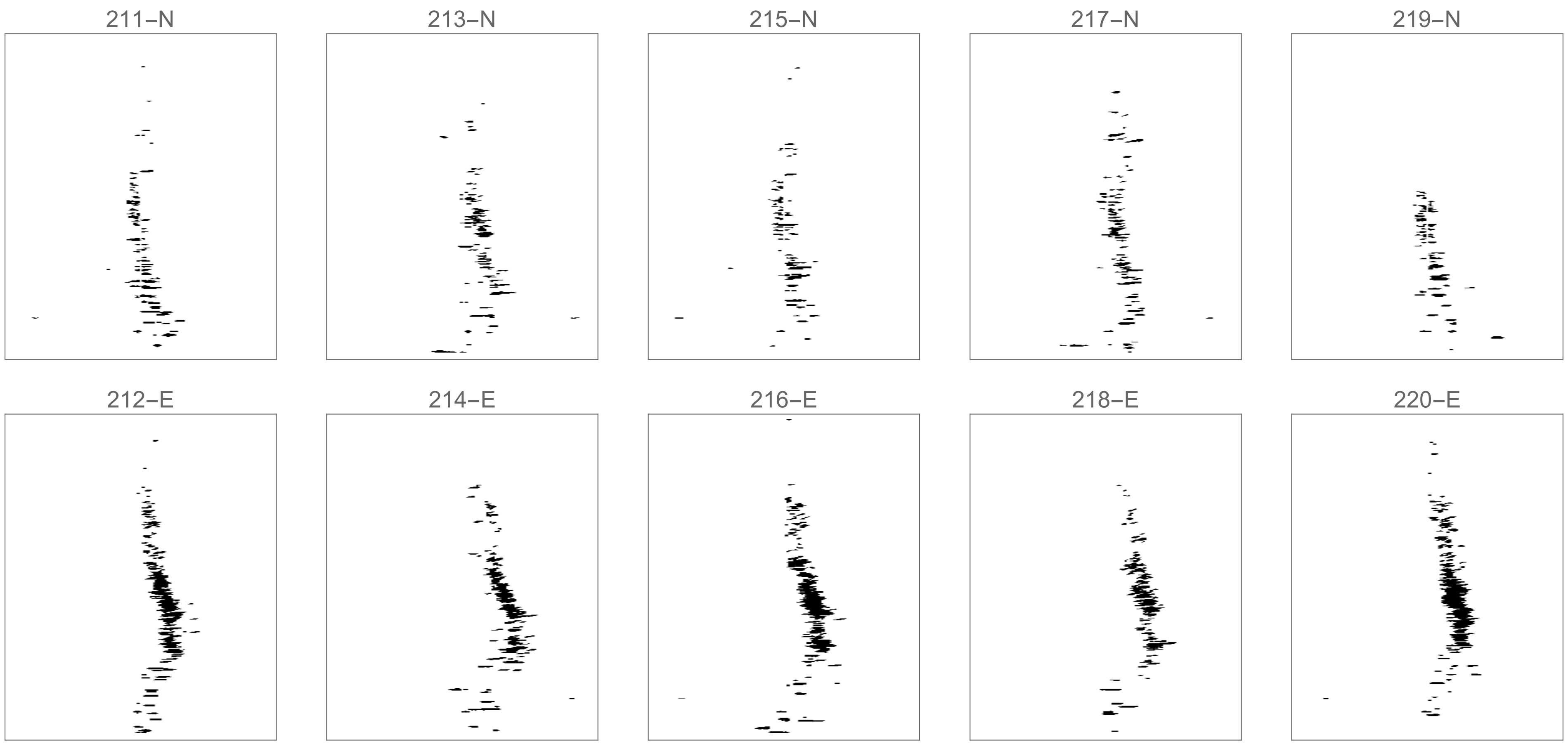

Nocturnal jets observed by WiPPR, group 1.

The horizontal axis in each figure is wind velocity (-40 to 40 m/s) and the vertical axis is altitude (0 to 1600 m). Each figure is an instantaneous measurement of a wind velocity component (east or north). Figures are separated by about 20 seconds in time. These data were measured at Yuma AZ on 28 June 2017 early in the morning. For the most part, radar backscatter is higher at the altitudes of highest wind speed. This is because the production of turbulence from wind shear is highest here. High turbulent intensity produces large changes in the electromagnetic index of refraction and correspondingly larger and more frequent radar echoes.

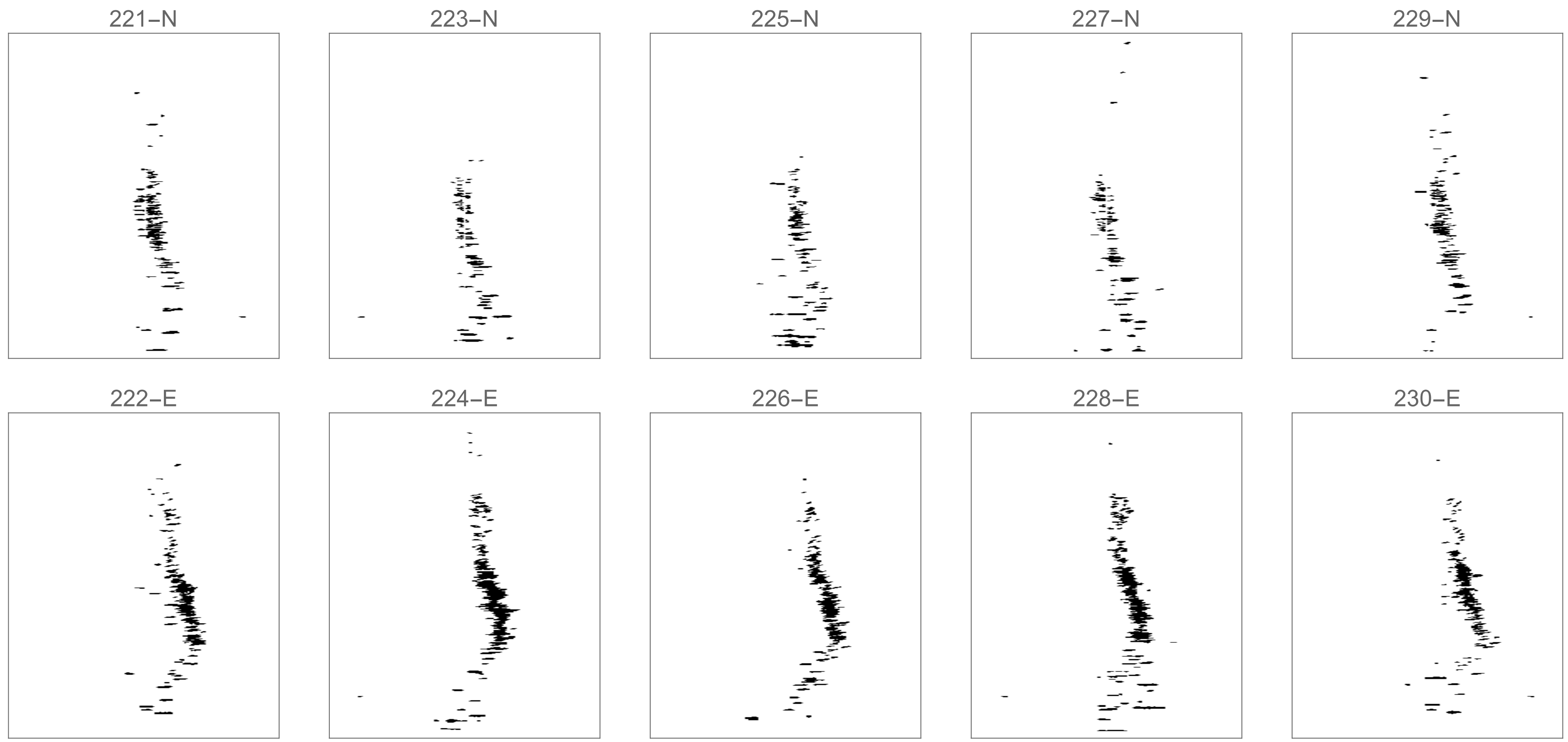

Nocturnal jets observed by WiPPR, group 2.

The horizontal axis in each figure is wind velocity (-40 to 40 m/s) and the vertical axis is altitude (0 to 1600 m). Each figure is an instantaneous measurement of a wind velocity component (east or north). Figures are separated by about 20 seconds in time. These data were measured at Yuma AZ on 28 June 2017 early in the morning. For the most part, radar backscatter is higher at the altitudes of highest wind speed. This is because the production of turbulence from wind shear is highest here. High turbulent intensity produces large changes in the electromagnetic index of refraction and correspondingly larger and more frequent radar echoes.

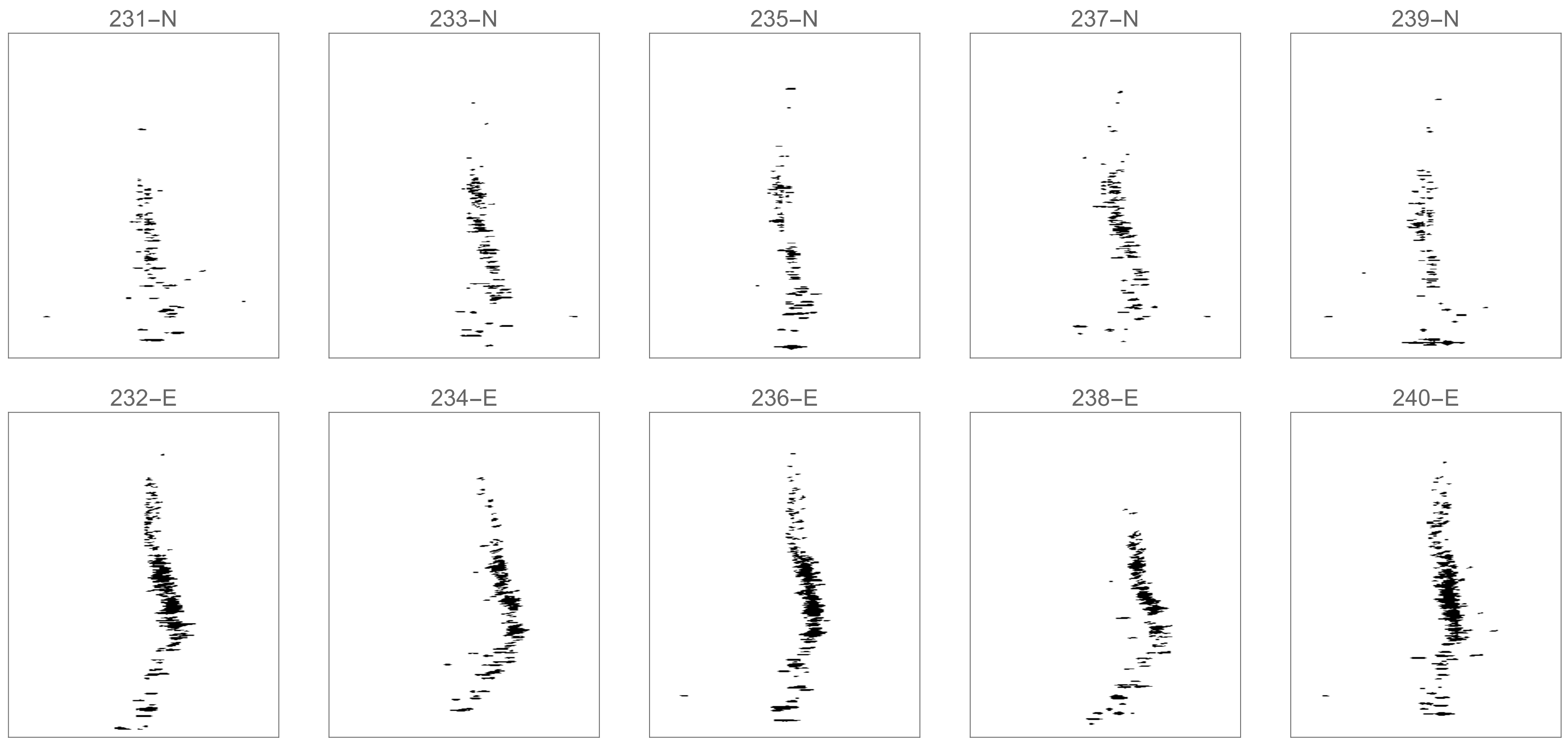

Nocturnal jets observed by WiPPR, group 3.

The horizontal axis in each figure is wind velocity (-40 to 40 m/s) and the vertical axis is altitude (0 to 1600 m). Each figure is an instantaneous measurement of a wind velocity component (east or north). Figures are separated by about 20 seconds in time. These data were measured at Yuma AZ on 28 June 2017 early in the morning. For the most part, radar backscatter is higher at the altitudes of highest wind speed. This is because the production of turbulence from wind shear is highest here. High turbulent intensity produces large changes in the electromagnetic index of refraction and correspondingly larger and more frequent radar echoes.

Gravity Waves

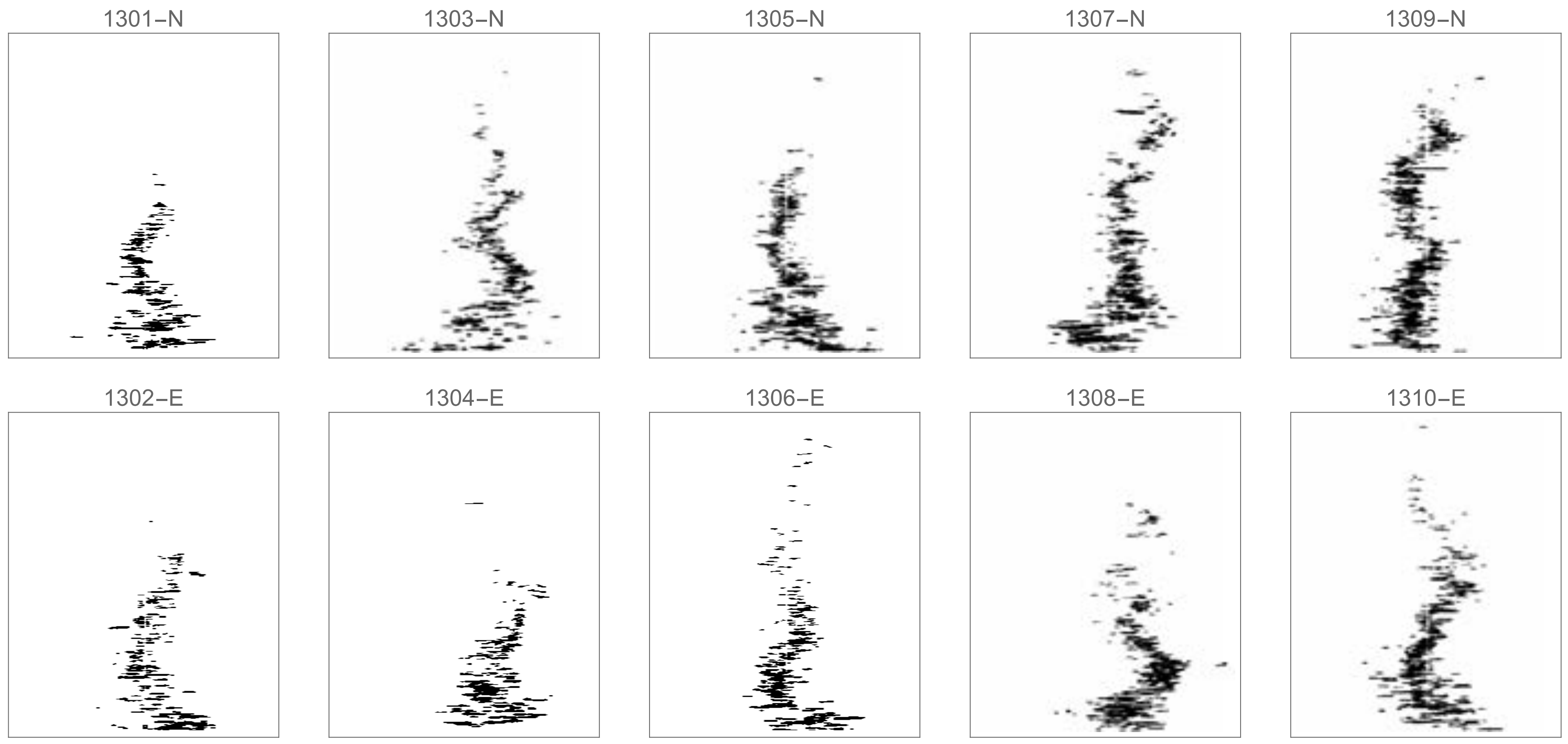

Gravity waves observed by WiPPR, group 1.

The horizontal axis in each figure is wind velocity (-40 to 40 m/s) and the vertical axis is altitude (0 to 1600 m). Each figure is an instantaneous measurement of a wind velocity component (east or north). Figures are separated by about 20 seconds in time. These data were measured at Yuma AZ on 28 June 2017 at midday. Notice how rapidly the winds vary with time and altitude.

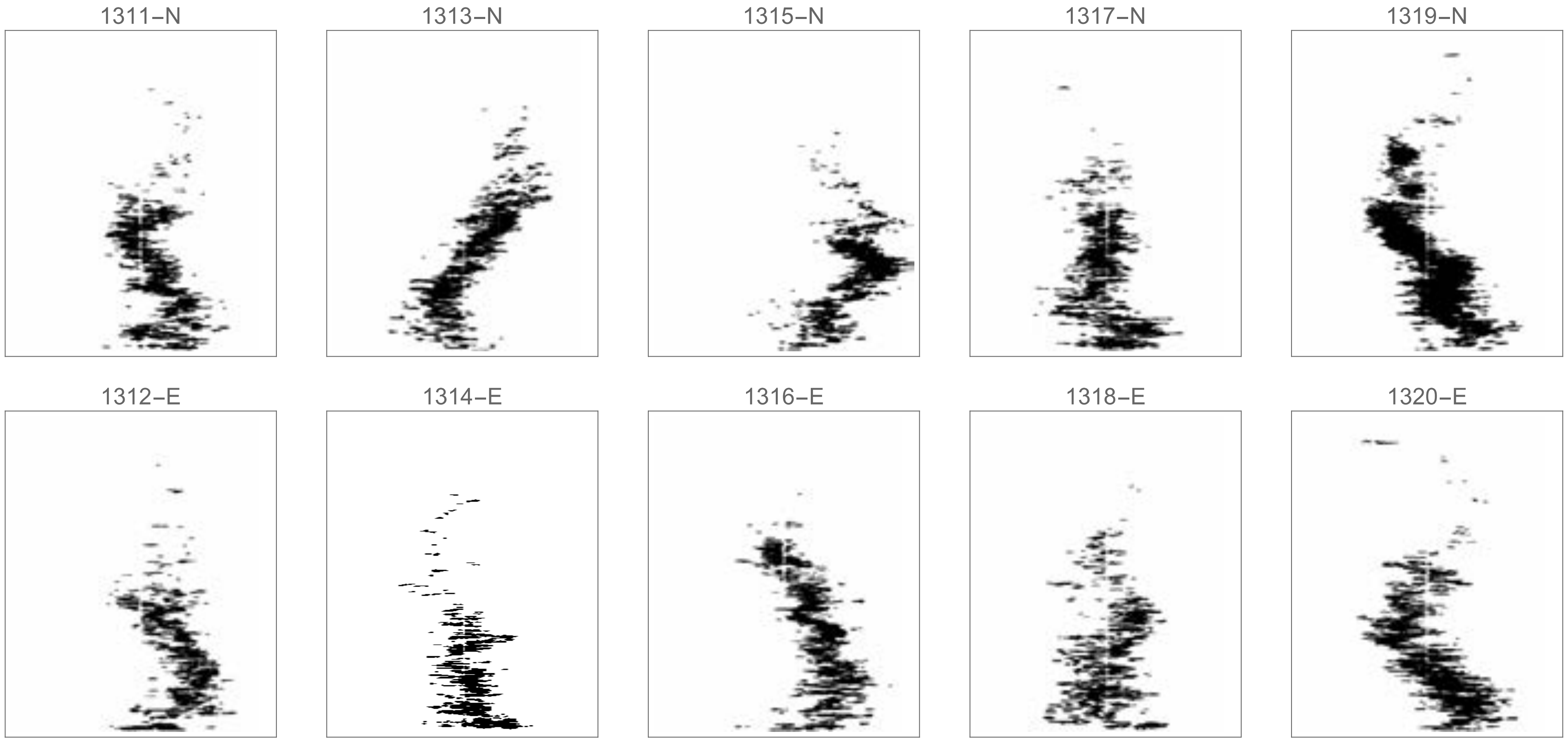

Gravity waves observed by WiPPR, group 2.

The horizontal axis in each figure is wind velocity (-40 to 40 m/s) and the vertical axis is altitude (0 to 1600 m). Each figure is an instantaneous measurement of a wind velocity component (east or north). Figures are separated by about 20 seconds in time. These data were measured at Yuma AZ on 28 June 2017 at midday. Notice how rapidly the winds vary with time and altitude.

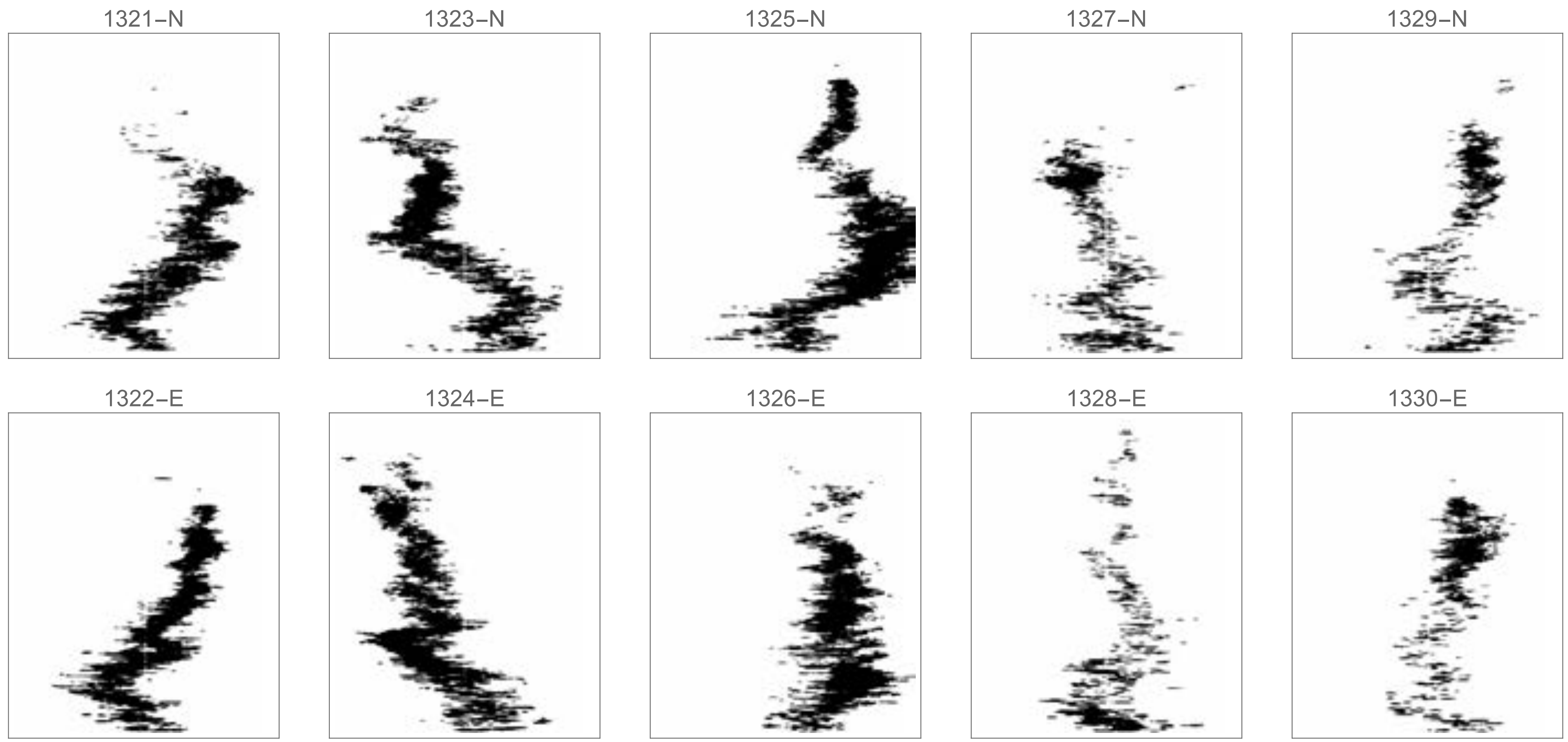

Gravity waves observed by WiPPR, group 3.

The horizontal axis in each figure is wind velocity (-40 to 40 m/s) and the vertical axis is altitude (0 to 1600 m). Each figure is an instantaneous measurement of a wind velocity component (east or north). Figures are separated by about 20 seconds in time. These data were measured at Yuma AZ on 28 June 2017 at midday. Notice how rapidly the winds vary with time and altitude.

Ekman Spiral

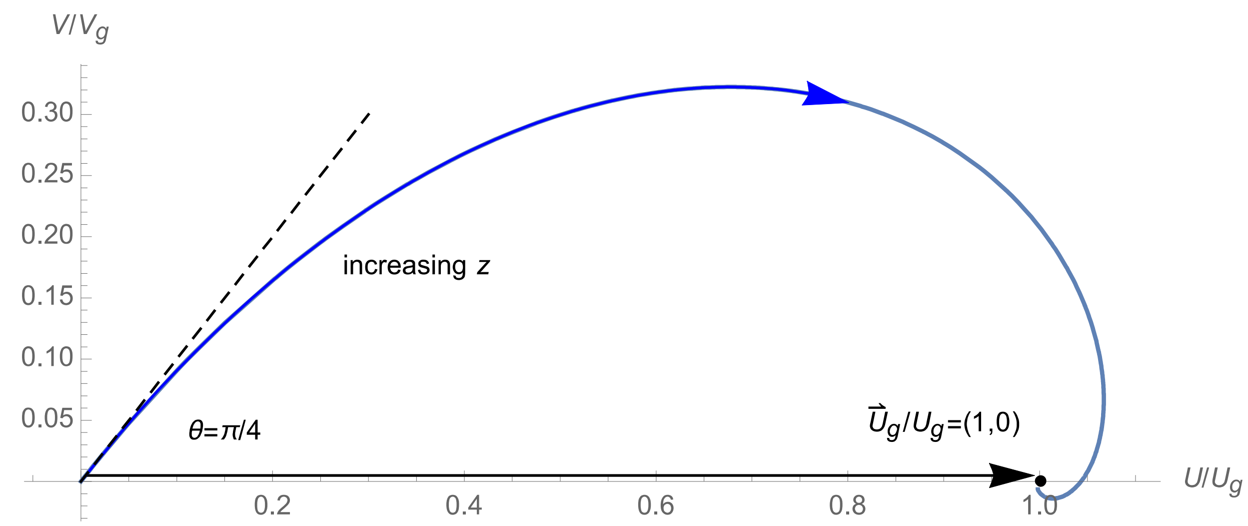

Ekman spiral in a neutral atmosphere.

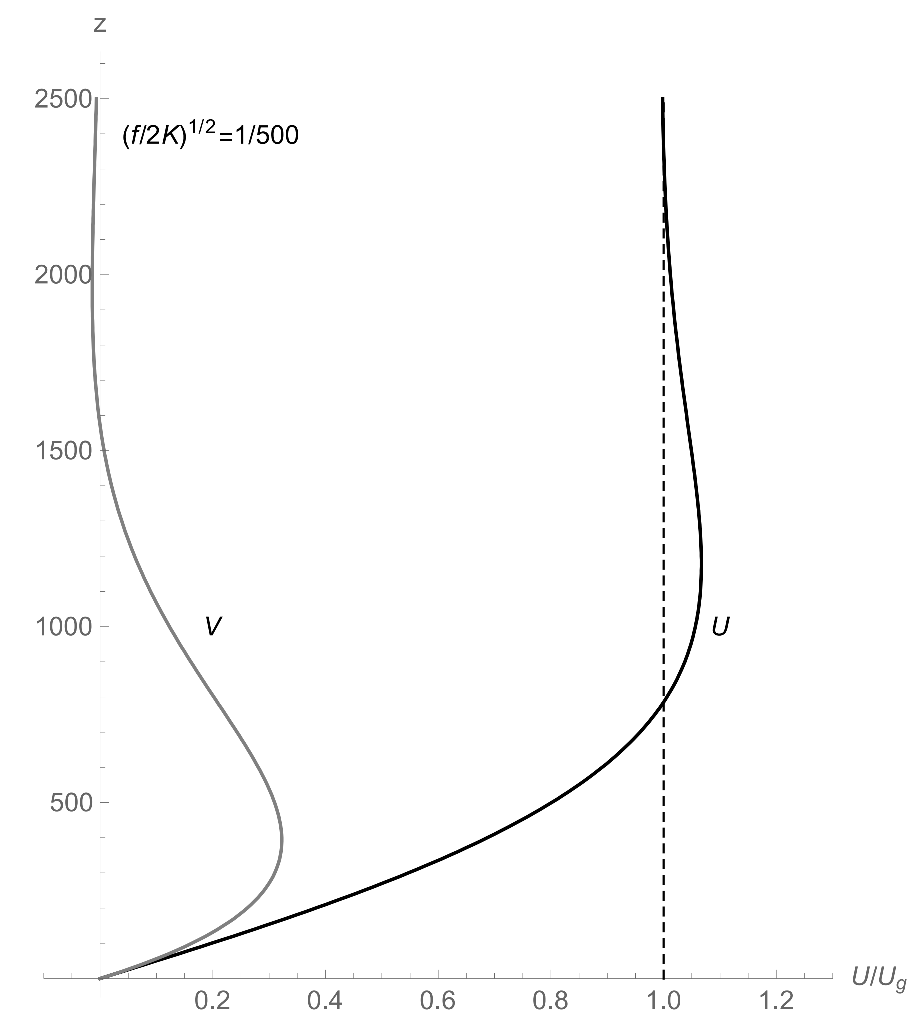

(Left) Wind hodograph. (Right) Variation of wind velocity with altitude. In a neutral atmosphere (no vertical mixing) the wind field is determined by a balance between geostrophic winds at high altitudes and friction effects at the earth's surface The result is a wind profile known known as an Ekman spiral. If the geostrophic winds are blowing from west to east at altitude then the wind direction will change by 45 deg as one descends towards the earth's surface. Pure neutral atmospheric conditions are rarely observed in practice for a variety of reasons including time scale and non uniform vertical eddy viscosity. Never the less, the Ekman spiral remains a useful model for interpreting variations in wind direction with height. The east and north component of wind speed are denoted by (u, v). The geostrophic winds at high altitudes are denoted by (u_g, v_g). The Coriolis parameter is f and K is the eddy diffusivity. The Ekman profile is

$$u(z) = u_g - \exp(-\gamma)(u_g \cos(\gamma z) + v_g \sin(\gamma z))$$

$$v(z) = v_g - \exp(-\gamma)(v_g \cos(\gamma z) - u_g \sin(\gamma z))$$

with $\gamma^2 = f/2K$.

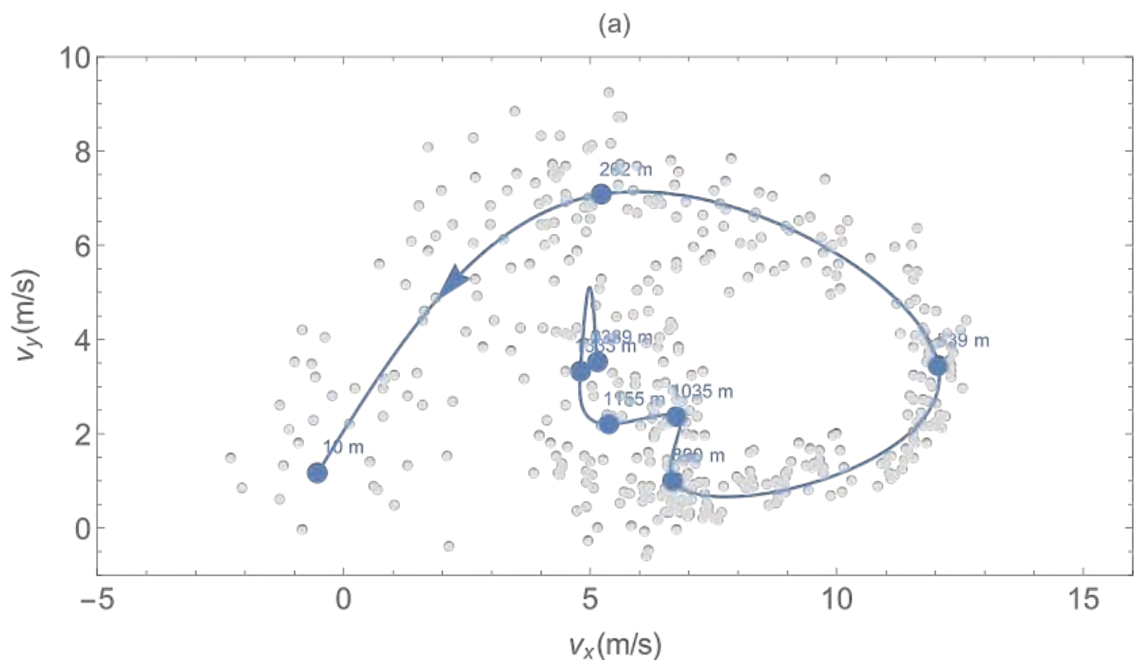

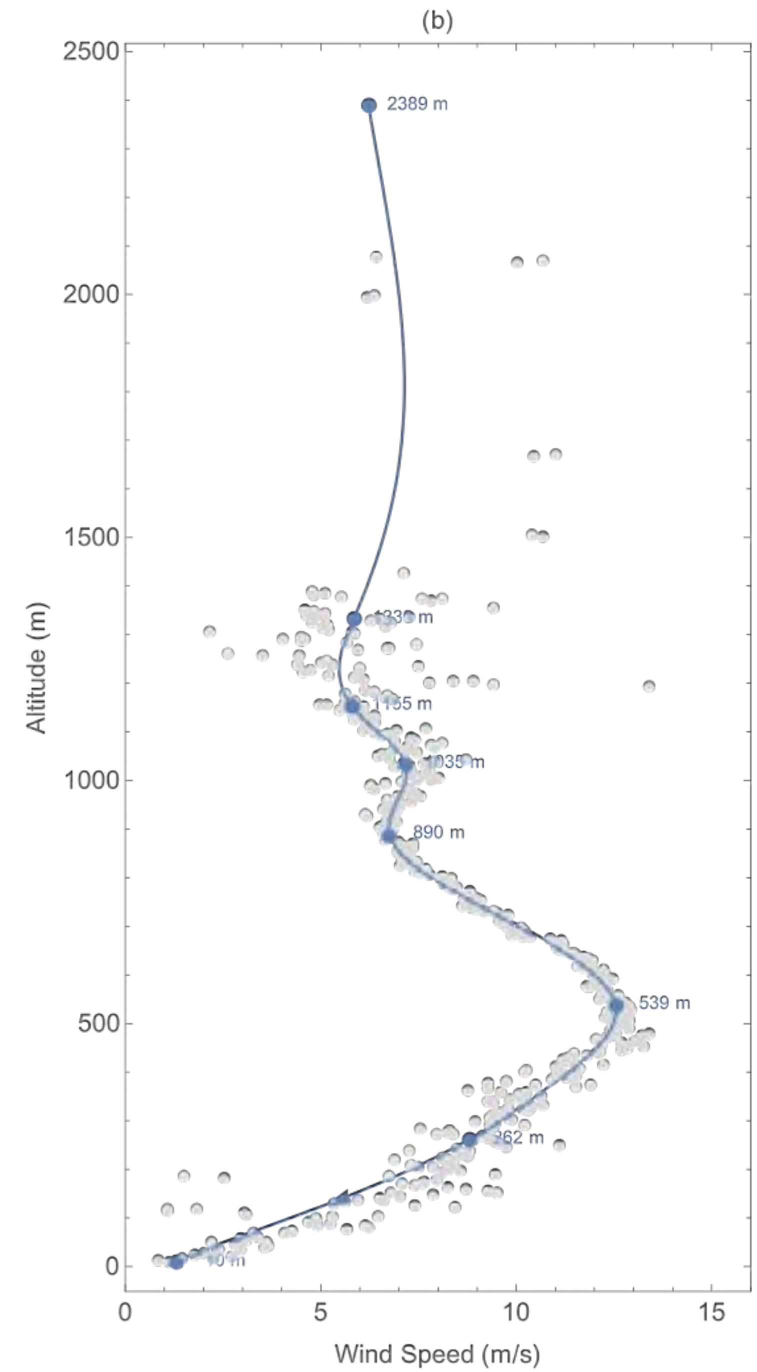

Wind direction and speed observed 28 June 2017

(a) Wind hododgraph, plots of (v_x,v_y) without regard to altitude. Below 890 m the wind changes in direction almost exactly like an ideal Ekman spiral with east moving geostrophic winds. Light gray points are the least squares four beam solution. Smooth blue curve is the global spline. (b) Wind speed versus altitude. The spline has been estimated using all measured data including altitudes where there is only a single Doppler measurement. Large blue points are the spline pivots with velocities converted to horizontal wind speed. The change in direction of the spiral is caused by ground friction effects. Below 1400 m (in the convective boundary layer) the agreement between the spline solution and the directly measured least squares solution is remarkable.

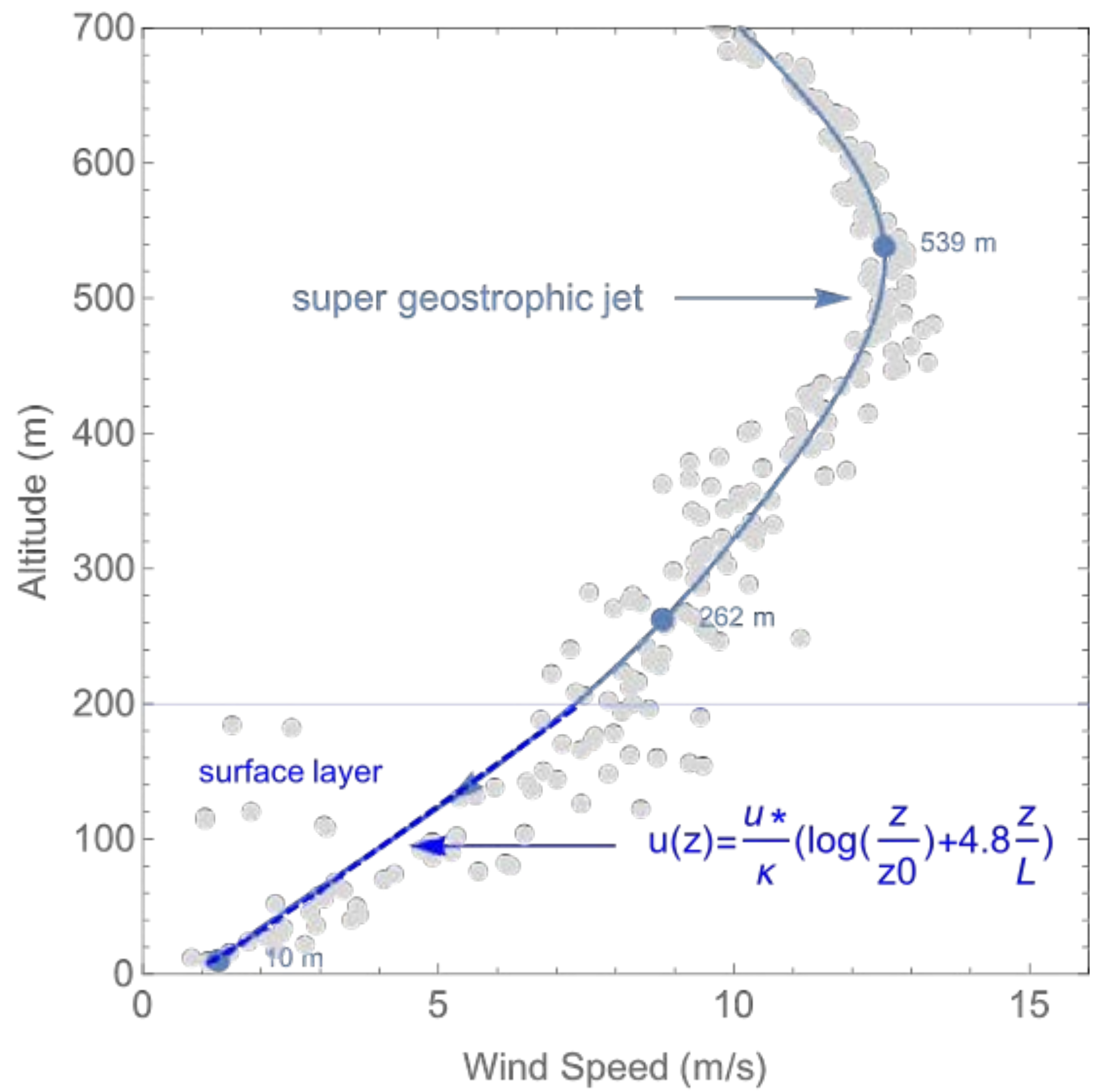

Application of Monin-Obukhov similarity theory.

The height of the surface layer has been estimated as 200 m. Wind speed data in this region has been fitted to a Monin-Obukhov similitude model assuming a stable atmosphere (see dashed blue line below 200 m). The form of the model is shown in the figure. Fitted friction velocity u^* and Obukhov length L for the model are u^*=0.048 m/s and L=18.6 m. L is positive in a stable atmosphere and negative in an unstable atmosphere. The fitted value is consistent with a stable atmosphere. The surface roughness has been estimated to be 0.01 m corresponding to rough soil. The bulge in wind speed near 500 m is a super geostrophic jet. Winds here are faster than the geostrophic winds at altitude. This is a carry over from the night time wind field. Later in the day wind speeds will typically be much slower at this altitude.

Points of Contact

Quinn Smith
QinetiQ Inc.
quinn.smith@us.qinetiq.com
(571)830-7440

Michael Vollmuth
Chief Operating Officer LogLinearGroup
michael.vollmuth@loglineargroup.com
(228)238-1496

Mark Henderson
Chief Engineer LogLinear Group
mark.henderson@loglineargroup.com
(228)697-2221

Marshall Bradley
Chief Scientist LogLinear Group
marshall.bradley@gmail.com
(985)290-4339

Website
https://loglineargroup.com